

Post-doctoral: Simulation and measurement of road surface  
optical properties

Ruqin Xiao

This work is under **REFLECTIVITY** project

## **Abstract**

**Abstract—**

**Key words—**

# Contents

<b>1</b>	<b>Introduction</b>	<b>4</b>
1.1	Context and objectives . . . . .	4
1.2	Mission . . . . .	5
1.3	Report organization . . . . .	6
<b>2</b>	<b>Optical properties of road surface</b>	<b>7</b>
2.1	Basic concepts . . . . .	7
2.1.1	Radiometric quantities . . . . .	7
2.1.2	Spectral radiometry . . . . .	8
2.2	Spectral BRDF . . . . .	9
2.2.1	Properties . . . . .	11
2.2.2	Isotropic and anisotropic . . . . .	12
2.3	Solar albedo . . . . .	12
2.3.1	Types of albedo . . . . .	12
2.3.2	The link between BRDF and solar albedo . . . . .	13
<b>3</b>	<b>BRDF models used in road surface</b>	<b>15</b>
3.1	Microfacet-based BRDF models . . . . .	16
3.1.1	Oren-Nayar BRDF . . . . .	17
3.1.2	Cook Torrance BRDF . . . . .	19
3.2	Lafortune BRDF . . . . .	22
3.3	Retro-phong BRDF . . . . .	23

3.4 Hapke's SHOE BRDF model . . . . .	23
<b>4 Measurements of Road Surface Optical Properties</b>	<b>26</b>
4.1 BRDF Measurements of Road Surface . . . . .	26
4.1.1 BRDF Measurement Set-up . . . . .	27
4.1.2 Overview of BRDF Measurement of Different Road Materials . . . . .	27
4.2 Solar Albedo Measurements of Road Surface . . . . .	38
4.2.1 Albedo Measurement set-up . . . . .	38
4.2.2 Overview of Solar Albedo Measurements on Road Surfaces . . . . .	41
<b>5 Simulation and Measurement of single-component road sample</b>	<b>42</b>
5.1 Methodology . . . . .	42
5.1.1 Preparation of single-material road samples . . . . .	42
5.1.2 Measurement set-up: the Gonioreflectometer at Cerema . . . . .	42
5.1.3 Fitting methods . . . . .	45
5.2 Results . . . . .	45
5.2.1 Result of Lazard 2/6 . . . . .	45
5.2.2 Result of Lazard 6/10 . . . . .	45
5.2.3 Result of Sand . . . . .	45
5.2.4 Result of . . . . .	45
<b>6 Simulation and measurement of multi-component road sample</b>	<b>46</b>
6.1 Existing methods of mixing BRDF . . . . .	46
6.2 Proposed methods . . . . .	46
6.3 Results . . . . .	46
6.3.1 Methodology . . . . .	46
6.3.2 Result of road sample 1 . . . . .	47
6.3.3 Result of road sample 2 . . . . .	47
6.3.4 Result of road sample 3 . . . . .	47
6.3.5 Result of road sample 4 . . . . .	47

<b>7 Conclusion and Perspectives</b>	<b>48</b>
7.1 Conclusion . . . . .	48
7.2 Perspectives . . . . .	48

# Chapter 1

## Introduction

### 1.1 Context and objectives

In our daily lives, we have seen a variety of road surfaces, including bituminous (or asphalt) roads, concrete roads, earthen roads, gravel roads, and murram roads. Among these, bituminous roads are the most commonly seen in our daily transportation due to their practicality, wear resistance and robustness. In the design and operation of mobility systems, many challenges, e.g. climate imperatives, the rise of active modes of transport, and the arrival of autonomous vehicles, require us to rethink a number of practices. In this context, the optical properties of road surface play a fundamental role in optimizing the energy consumption of public lighting installations [1], reduce light pollution [2], control urban temperature [3], and consider perception of road markings [4]. In favor of these issues, it becomes necessary to know the optical properties of road surface or be able to anticipate them when creating a surfacing or predicting their evolution over time. Consequently, this requires conducting a significant number of simulations or measurements.

When discussing optical properties of road surface, both the Bidirectional Reflectance Distribution Function (BRDF) and solar albedo are essential because they provide complementary information about how the surface interacts with light. The former provides detailed directional information, describing the angular distribution of reflected light based on the angle of incoming light and the viewing angle [5]. It captures how surface roughness, texture, and material composition affect

light reflection, affecting the visibility of the road and markings [6]. The latter gives an overall measure of reflected energy, representing the total fraction of incoming solar energy reflected by the road surface, without regard to direction [7]. Road surface with higher solar albedo reduces heat absorption by reflecting more sunlight back into the atmosphere, lowering cooling demands in nearby buildings and contributing to mitigate the damage on road materials.

These two properties depend on the physical characteristics of the road surface, such as roughness and refractive index. However, the measurement of BRDF or solar albedo is costly, not only in terms of instrumentation but also in the time required to measure it. This raises the question: if we already know the physical characteristics of a road surface, is it possible to derive its BRDF and solar albedo without direct measurement? Specifically, if we have a road sample and know its formulation in terms of the material composition, sizes, and proportions. Can we establish a reliable relationship between these parameters and the resulting optical properties? However, the challenge lies in the fact that the relationship between the formulation of a road surface and its corresponding characteristics is not explicitly defined, complicating numerical simulation of the BRDF and so solar albedo. Roads are typically composed of various materials, such as bitumen, different types of aggregates, and fillers, which further adds to the complexity.

To simplify the problem, we propose to focus firstly on several single-component road samples to investigate appropriate BRDF models that can accurately fit their measured results. So the problem becomes how to combine these BRDF models for each single-component to fit the measured BRDF of multi-component road sample. To explore and develop such methods is the objective of this work.

## 1.2 Mission

To achieve the objective, the mission follows 5 steps:

1. Build several single-component road samples and measure their BRDF;
2. Fit the measured BRDF of each single-component road sample using existing BRDF models;
3. Build several multi-component road samples and measure their BRDF;

4. Explore and develop the method to combine the BRDFs of each single-component to fit the measurement of multi-component road samples;
5. Estimate the solar albedo using BRDF.

### **1.3 Report organization**

This report is structured into the following chapters:

# Chapter 2

## Optical properties of road surface

### 2.1 Basic concepts

To provide a clear understanding of the optical properties of road surface, the fundamental terminologies are introduced in this section.

#### 2.1.1 Radiometric quantities

Radiometric quantities provide a way to measure and describe the behavior of radiant energy in terms of light interaction with road surface. They include flux, radiant intensity, irradiance and radiance.

**Flux**  $F$ , is the most fundamental quantity in radiometry [5]. It is also called radiant power, which measures the amount of light that hits a surface over a finite area from all directions per unit time. For a given amount of radiated energy  $Q$  at a time duration  $t$ , the flux  $F$  is expressed as:

$$F(t) = \frac{dQ}{dt} \quad (2.1)$$

As  $Q$  is expressed in Joules ( $J$ ), the unit of  $F$  is watts ( $W = J \cdot s^{-1}$ )

**Radiant intensity**  $I$ , is a correlated measure of flux. It represents the intensity of flux per unit solid angle which is propagate towards some specific direction  $(\theta, \varphi)$  toward the the infinitesimal

solid angle  $d\vec{\omega}$  [8]. Thus, it can be expressed in terms of flux:

$$I(t, \theta, \varphi) = \frac{dF(t)}{d\vec{\omega}} = \frac{dF(t)}{\sin \theta d\theta d\varphi} \quad (2.2)$$

Notice that the unit of solid angle is the steradian [ $sr$ ], so the unit of radiant intensity is [ $W \cdot sr^{-1}$ ].

**Irradiance**  $E$ , is another correlated measure of flux in terms of surface area. Different from radiant intensity, it captures the integration over the entire hemisphere  $\Omega$  of the incident light arriving at a unit surface  $ds(x)$  centered on the point  $x$ . Essentially, it measures the amount of radiated energy strike a unit area per unit time:

$$E(x, t) = \frac{dF(t)}{ds(x)} \quad (2.3)$$

Its unit is [ $W \cdot m^{-2}$ ]

**Radiance**  $L$ , measures the amount of incident light arriving at a unit surface  $ds(x)$  centered on  $x$  from a unit solid angle  $d\vec{\omega}$  per unit time  $t$ . It can be considered as a correlated measure of radiant intensity per unit area or irradiance per unit solid angle:

$$L(x, t, \theta, \varphi) = \frac{d^2F(t)}{|\vec{\omega} \cdot \vec{n}| d\vec{\omega} ds(x)} = \frac{dI(t, \theta, \varphi)}{\cos \theta ds(x)} = \frac{dE(x, t)}{\sin \theta d\theta d\varphi} \quad (2.4)$$

The product term  $\cos \theta ds(x)$  represents the projection of the unit surface  $ds(x)$  onto the direction  $\vec{\omega}$ . According to its definition, the unit of  $L(x, t, \theta, \varphi)$  is [ $W \cdot m^{-2} \cdot sr^{-1}$ ].

### 2.1.2 Spectral radiometry

In the previous section, the definitions of radiometric quantities are given without considering the wavelength. In order to describe the spectral distribution of a radiation, the spectral radiometric quantities are introduced, including spectral flux, spectral intensity, spectral irradiance and spectral radiance.

**Spectral flux**  $F_\lambda$ , is defined as the flux per unit wavelength and expressed in [ $W \cdot nm^{-1}$ ]:

$$F_\lambda(t) = \frac{dF(t)}{d\lambda} \quad (2.5)$$

**Spectral intensity**  $I_\lambda$ , is the radiant intensity per unit wavelength and expressed in [ $W \cdot sr^{-1} \cdot nm^{-1}$ ]:

$$I_\lambda(t, \theta, \varphi) = \frac{dI(t, \theta, \varphi)}{d\lambda} \quad (2.6)$$

**Spectral irradiance**  $E_\lambda$ , is irradiance per unit wavelength and expressed in [ $W \cdot m^{-2} \cdot nm^{-1}$ ]:

$$E_\lambda(x, t) = \frac{E(x, t)}{d\lambda} \quad (2.7)$$

**Spectral radiance**  $L_\lambda$ , is defined as the radiance per unit wavelength and expressed in [ $W \cdot m^{-2} \cdot sr^{-1} \cdot nm^{-1}$ ]:

$$L_\lambda(x, t, \theta, \varphi) = \frac{dL(x, t, \theta, \varphi)}{d\lambda} \quad (2.8)$$

The measurement of spectral quantities are conducted with instruments such as spectrophotometers which analyze the radiation in adjacent and narrow spectral bands [8]. When analyzing radiation over a broader wavelength range  $[\lambda_1, \lambda_2]$ , the total measured flux can be calculated by integrating the spectral flux density across the specified waveband. This process accounts for the contribution of all individual wavelengths within the range, providing a cumulative representation of the flux. The computation is expressed as:

$$F(\lambda_1, \lambda_2) = \int_{\lambda_1}^{\lambda_2} F_\lambda d\lambda \quad (2.9)$$

## 2.2 Spectral BRDF

The BRDF is first introduced by Fred Nicodemus in 1965 [9], which is rigorously defined as the ratio of reflected radiance in a given viewing direction to the incident irradiance from a specified light source direction, at a given surface point  $x$ . It is typically expressed in units of  $sr^{-1}$ . However, the BRDF alone does not capture the full complexity of how surfaces reflect light across different wavelengths. To gain a more comprehensive understanding of these interactions, we turn to the spectral BRDF which is an extension of the traditional BRDF [8]. It provides a wavelength-dependent function that characterizes how surfaces reflect light at specific incident and reflected angles at a given surface point  $x$ , across a narrow spectral bandwidth  $\Delta\lambda$ . Mathematically, it is expressed as:

$$f_r(x, \lambda, \theta_i, \varphi_i, \theta_r, \varphi_r) = \frac{dL(x, \lambda, \theta_r, \varphi_r)}{dE(x, \lambda, \theta_i, \varphi_i)}, \quad (2.10)$$

where:

- $\lambda$  is the wavelength of light source;

- $\theta_i$  and  $\varphi_i$  are the zenith and azimuth angle of the unit incident direction  $\vec{\omega}_i$ :

$$\vec{\omega}_i = (x_i, y_i, z_i) = (\sin \theta_i \cos \varphi_i, \sin \theta_i \sin \varphi_i, \cos \theta_i)$$

- $\theta_r$  and  $\varphi_r$  are the zenith and azimuth angle of the unit reflected direction  $\vec{\omega}_r$ :

$$\vec{\omega}_r = (x_r, y_r, z_r) = (\sin \theta_r \cos \varphi_r, \sin \theta_r \sin \varphi_r, \cos \theta_r)$$

- $dL(x, \lambda, \theta_r, \theta_r)$  is the spectral reflected radiance for waveband  $\Delta\lambda$ ;

$$dL(x, \lambda, \theta_r, \theta_r) = \int_{\Delta\lambda} dL_\lambda(x, \theta_r, \varphi_r) d\lambda$$

- $dE(x, \lambda, \theta_i, \varphi_i)$  is the spectral incident irradiance for waveband  $\Delta\lambda$ .

$$dE(x, \lambda, \theta_i, \theta_i) = \int_{\Delta\lambda} dE_\lambda(x, \theta_i, \varphi_i) d\lambda$$

Replacing the term  $dE(x, \lambda, \theta_i, \varphi_i)$  according to Equation (2.4), it can be defined in terms of incident radiance  $L_i(x, \lambda, \theta_i, \varphi_i)$ :

$$f_r(x, \lambda, \theta_i, \varphi_i, \theta_r, \varphi_r) = \frac{dL(x, \lambda, \theta_r, \theta_r)}{\cos \theta_i L_i(x, \lambda, \theta_i, \varphi_i) d\theta_i d\varphi_i} \quad (2.11)$$

As both radiance and irradiance take into account the wavelength, the unit of spectral BRDF is still  $[sr^{-1}]$ .

### Ideal diffuse reflection

One of the simplest and most widely used BRDF models is the Lambertian reflector, which is based on the assumption of a perfectly diffuse surface [8]. It has an angle-independent BRDF, proportional to their spectral albedo  $\rho(\lambda)$ :

$$f_{r(difuse)}(x, \lambda, \theta_i, \varphi_i, \theta_r, \varphi_r) = \frac{\rho(\lambda)}{\pi} \quad (2.12)$$

### Ideal specular reflection

In contrast to diffuse reflection, the perfect specular BRDF describes light incoming a given direction is reflected in a single direction following the law of reflection [10]:

$$f_{r(specular)}(x, t, \theta_i, \varphi_i, \theta_r, \varphi_r) = F_r(\theta_i) \frac{\delta(\vec{\omega}_r - \vec{\omega}_r)}{\cos \theta_r}, \quad (2.13)$$

where:

- $\vec{\omega}'_r$  is the mirror direction which is symmetric to the incoming direction  $\vec{\omega}_i$ :

$$\vec{\omega}'_r = 2(\vec{\omega}_i \cdot \vec{n})\vec{n} - \vec{\omega}_i = 2 \cos \theta_i \vec{n} - \vec{\omega}_i$$

- $\delta(\vec{\omega}_r - \vec{\omega}'_r)$  is the delta dirac function;
- $F_r(\theta_i)$  is the Fresnel reflectance following as:

$$F_r(\theta_i, \varphi_i) = \frac{1}{2} (r_{\parallel}^2 + r_{\perp}^2)$$

$r_{\parallel}$  and  $r_{\perp}$  are the conventional Fresnel coefficient [11].

### 2.2.1 Properties

Similar to traditional BRDF, a physically plausible spectral BRDF also has the below properties:

- **Energy conservation**

A fundamental principle that must be adhered to by all BRDFs, including spectral BRDFs, is energy conservation. This ensures that the amount of light reflected by a surface does not exceed the amount of light incident upon it. Mathematically, this is often represented as:

$$\int_{\varphi_i=0}^{2\pi} \int_{\theta_i=0}^{\frac{\pi}{2}} f_r(x, \lambda, \theta_i, \varphi_i, \theta_r, \varphi_r) \cos(\theta_r) \sin(\theta_r) d\theta_r d\varphi_r \leq 1$$

- **Reciprocity**

The Helmholtz Reciprocity Rule states that the reflection characteristics should remain unchanged if the directions of light incidence and observation are swapped:

$$f_r(x, \lambda, \theta_i, \varphi_i, \theta_r, \varphi_r) = f_r(x, \lambda, \theta_r, \varphi_r, \theta_i, \varphi_i)$$

It ensures that light behaves consistently in all directions.

- **Non-negative**

The spectral BRDF is always non-negative, ensuring that the reflected radiance is physically meaningful:

$$f_r(x, \lambda, \theta_i, \varphi_i, \theta_r, \varphi_r) \geq 0$$

## 2.2.2 Isotropic and anisotropic

As spectral BRDF is an extension of traditional BRDF, it can be classified into two categories based on whether they exhibit rotational symmetry or not [10,12]: isotropic and anisotropic. A material is considered isotropic when its reflectance remains constant for a fixed view and illumination, regardless of the rotation of the material around its normal. Mathematically, it can be expressed in term of the azimuth angle difference between incident direction and reflected direction:

$$f_r(x, \lambda, \theta_i, \varphi_i, \theta_r, \varphi_r) = f_r(x, \lambda, \theta_i, \theta_r, \varphi_r - \varphi_i)$$

In contrast, materials whose reflectance is not constant are considered anisotropic.

## 2.3 Solar albedo

Another important optical property of road surface, solar albedo (also called solar reflectance) is introduced and discussed in this section.

### 2.3.1 Types of albedo

Solar albedo of a given surface is defined as the ratio of upward and downward radiation flux [13,14]. This ratio can vary between 0 and 1, where 0 indicates no reflection and 1 signifies complete reflection. Surfaces with higher albedo values reflect more sunlight, leading to cooler temperatures, while those with lower values absorb more radiation, resulting in higher temperatures. As such, it becomes an important factor affecting the temperature of a sunlit surface and that of near-surface ambient air temperature.

There are three primary types of albedo [13] that are commonly discussed, each with distinct implications for environmental and climatic conditions.

#### 1. Black sky albedo

When the surface is illuminated with ideal directional radiation, the surface albedo is called black-sky albedo or directional-hemispherical reflectance:

$$\alpha_{black-sky}(\lambda, \vec{\omega}_i) = \frac{\int_{\Omega} L_{\lambda}(\vec{\omega}_r) d\vec{\omega}_r}{E_{\lambda}(\vec{\omega}_i)} \quad (2.14)$$

Where  $L_\lambda$  is the reflected radiance in the direction  $\vec{\omega}_r$ , and  $E_\lambda$  is the incident irradiance from the direction  $\vec{\omega}_i$ .

## 2. White sky albedo

When the surface is illuminated with ideal diffuse radiation, the surface albedo is called white-sky albedo or bi-hemispherical reflectance:

$$\alpha_{white-sky}(\lambda) = \frac{\int_{\Omega} L_\lambda(\vec{\omega}_r) d\vec{\omega}_r}{E_\lambda} \quad (2.15)$$

Different from the term  $E_\lambda$  in black-sky albedo, here it represents the incident irradiance from all directions into the hemisphere.

## 3. Blue sky albedo

In fact, the solar albedo we measured is usually under natural daylight illumination, including both directional and diffuse radiation. In this case, the surface albedo is called as blue-sky albedo, which can be approximately expressed as a linear combination of black-sky and white-sky albedo:

$$\alpha_{blue-sky}(\lambda, \vec{\omega}_i) \approx (1 - D(\tau, \lambda))\alpha_{black-sky}(\lambda, \vec{\omega}_i) + D(\tau, \lambda)\alpha_{white-sky}(\lambda) \quad (2.16)$$

Where  $D(\tau, \lambda)$  gives the fraction of the diffuse radiation, varying with the aerosol optical wavelength  $\tau$  and wavelength  $\lambda$ .

For a given waveband, its corresponding surface albedo can be estimated using the following equation:

$$\alpha(\vec{\omega}_i) = \frac{\int_{\lambda_1}^{\lambda_2} E_\lambda(\vec{\omega}_i) \alpha_\lambda(\vec{\omega}_i) d\lambda}{\int_{\lambda_1}^{\lambda_2} E_\lambda(\vec{\omega}_i) d\lambda} \quad (2.17)$$

### 2.3.2 The link between BRDF and solar albedo

According to the definition of BRDF, black-sky albedo and white sky albedo, we can find the link between them. The black-sky albedo can be derived by integrating BRDF over the viewing hemisphere:

$$\alpha_{black-sky}(\lambda, \theta_i, \varphi_i) = \int_{\varphi_r=0}^{2\pi} \int_{\theta_r=0}^{\frac{\pi}{2}} f_r(\lambda, \theta_i, \varphi_i, \theta_r, \varphi_r) \cos \theta_r \sin \theta_r d\theta_r d\varphi_r \quad (2.18)$$

Similarly, the white-sky albedo can be derived by integrating BRDF over the viewing hemisphere and incident hemisphere:

$$\alpha_{white-sky}(\lambda) = \frac{1}{\pi} \int_{\varphi_i=0}^{2\pi} \int_{\theta_i=0}^{\frac{\pi}{2}} \int_{\varphi_r=0}^{2\pi} \int_{\theta_r=0}^{\frac{\pi}{2}} f_r(\lambda, \theta_i, \varphi_i, \theta_r, \varphi_r) \cos \theta_i \sin \theta_i \cos \theta_r \sin \theta_r d\theta_i d\varphi_i d\theta_r d\varphi_r \quad (2.19)$$

For ideal diffuse reflection, we can conclude that the black-sky albedo and the white-sky albedo are equivalent to the albedo  $\rho$  used in Equation 2.12 by computing these two equations.

# Chapter 3

## BRDF models used in road surface

Reflectance models are typically introduced in order to achieve low-parameter representation of the BRDF measurements acquired from road surfaces [6]. Many road surfaces exhibit non-diffuse characteristics, simplified Lambertian assumptions are insufficient for accurate optical predictions. This is especially true for surfaces that include specular peaks due to polishing or for materials that have retro-reflective properties, such as in tunnel markings or retro-reflective coatings [15]. To address these complexities, this chapter explores a range of reflectance models utilized for characterizing the BRDF of various road materials, such as concrete, sand, aggregates.

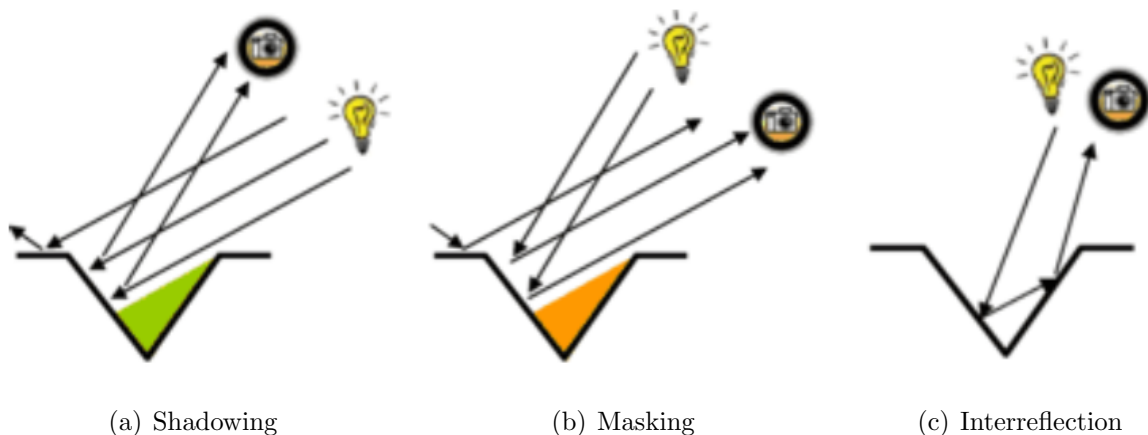


Figure 3.1: Physical phenomena in microfacets

### 3.1 Microfacet-based BRDF models

This section introduces two widely used reflectance models used in road surface: Oren-Nayar (ON) BRDF and Cook-Torrance (CT) BRDF. Both are based on microfacet theory which represents the surface of a collection of small surfaces. In graphics community, microfacet theory was used to derive physically based BRDF [16], and typically accounts for complex geometric and radiometric phenomena:

- shadowing, where the facet is only partially illuminated because the adjacent facet casts a shadow on it, as seen in Fig. 3.1(a);
- masking, where the facet is only partially visible to the camera because its adjacent facet occludes it, as seen in Fig. 3.1(b).

Their impacts are described using shadowing function and masking function, respectively. A meaningful microfacet model is described by a distribution of normals, which models how the microfacets are statistically oriented, and a microfacet profile, which models how the microfacets are organized on the microfacet. Mathematically, the general microfacet-based BRDF expression is following as:

$$f_r(\vec{\omega}_i, \vec{\omega}_r) = \frac{1}{\cos(\theta_r) \cos(\theta_i)} \int_{\Omega} f_{r(M)}(\vec{\omega}_i, \vec{\omega}_r, \vec{\omega}_m)(\vec{\omega}_r \cdot \vec{\omega}_m)(\vec{\omega}_i \cdot \vec{\omega}_m)G(\vec{\omega}_i, \vec{\omega}_r, \vec{\omega}_m)D(\vec{\omega}_m)d\vec{\omega}_m, \quad (3.1)$$

where:

- $\vec{\omega}_i, \vec{\omega}_r, \vec{\omega}_m$  are the directions of the incident light, detection and the normal of the microfacet;
- $f_{r(M)}(\vec{\omega}_i, \vec{\omega}_r, \vec{\omega}_m)$  is the BRDF of each microfacet;
- $D(\vec{\omega}_m)$  represents the distribution of the normals of the microfacets;
- $G(\vec{\omega}_i, \vec{\omega}_r, \vec{\omega}_m)$  is geometric attenuation function, combining masking  $G_1$  and shadowing  $G_2$  function. It gives the fraction of microfacets with normal  $\omega_m$  that are visible along the reflected direction  $\vec{\omega}_r$ , depending on the microfacet profile (e.g. V-cavity microfacet profile and smith microfacet profile) and the distribution of the microfacet's normal [16]. The

masking  $G_1$  and shadowing  $G_2$  function are formalized by the following equations:

$$\begin{aligned}\cos \theta_r &= \int_{\Omega} G_1(\vec{\omega}_r, \vec{\omega}_m)(\vec{\omega}_r \cdot \vec{\omega}_m) D(\vec{\omega}_m) d\vec{\omega}_m \\ \cos \theta_i &= \int_{\Omega} G_2(\vec{\omega}_i, \vec{\omega}_m)(\vec{\omega}_i \cdot \vec{\omega}_m) D(\vec{\omega}_m) d\vec{\omega}_m\end{aligned}\quad (3.2)$$

### 3.1.1 Oren-Nayar BRDF

The Oren-Nayar BRDF is widely used for modelling diffuse reflections from rough surfaces, as it provides a more realistic representation of light behavior compared to simpler Lambertian model [6, 17, 17]. This model was first proposed in 1994 [17] by Oren and Nayar, based on microfacet theory adapting V-cavity microfacet profile. More precisely, the surface is assumed as a collection of long, symmetric v-shaped cavities with equal length, each containing two opposing planar facets, as seen in Fig. ?? This implies that each V-cavity has the two symmetric normals,  $\vec{\omega}_m$  and  $\vec{\omega}'_m$  leading to the following distribution of normals of each microfacet:

$$D(\vec{\omega}) = \frac{1}{2} \frac{\delta(\vec{\omega} - \vec{\omega}_m)}{\vec{\omega}_m \cdot \vec{n}} + \frac{1}{2} \frac{\delta(\vec{\omega} - \vec{\omega}'_m)}{\vec{\omega}'_m \cdot \vec{n}}$$

The masking or shadowing term can be derived according to Equation(3.2) considering if there is no or one backfacing normal direction:

$$\begin{aligned}G_1(\vec{\omega}_r, \vec{\omega}_m) &= \min \left( 1, 2 \frac{(\vec{\omega}_m \cdot \vec{n})(\vec{\omega}_r \cdot \vec{n})}{(\vec{\omega}_r \cdot \vec{\omega}_m)} \right) \\ G_2(\vec{\omega}_i, \vec{\omega}_m) &= \min \left( 1, 2 \frac{(\vec{\omega}_m \cdot \vec{n})(\vec{\omega}_i \cdot \vec{n})}{(\vec{\omega}_i \cdot \vec{\omega}_m)} \right)\end{aligned}$$

Considering both masking and shadowing, the term  $G(\vec{\omega}_i, \vec{\omega}_r, \vec{\omega}_m)$  can be derived as:

$$G(\vec{\omega}_i, \vec{\omega}_r, \vec{\omega}_m) = \min \left( 1, 2 \frac{(\vec{\omega}_m \cdot \vec{n})(\vec{\omega}_r \cdot \vec{n})}{(\vec{\omega}_r \cdot \vec{n})}, 2 \frac{(\vec{\omega}_m \cdot \vec{n})(\vec{\omega}_i \cdot \vec{n})}{(\vec{\omega}_i \cdot \vec{n})} \right) \quad (3.3)$$

The distribution of the normals of all microfacets is described using a spherical gaussian distribution with a mean value of zero and a standard deviation  $\sigma$ , which serves as a roughness parameter:

$$D(\vec{\omega}_m) = ce^{-\frac{\theta_m^2}{2\sigma^2}}, \quad (3.4)$$

where the normalization constant  $c$  is:

$$c = \frac{1}{\int_{\varphi_m=0}^{2\pi} \int_{\theta_m}^{\frac{\pi}{2}} e^{-\frac{\theta_m^2}{2\sigma^2}} \sin \theta_m d\theta_m d\varphi_m}$$

Besides, the facets are assumed to exhibit diffuse reflection, implying the BRDF of each microfacet  $f_{r(M)}(\vec{\omega}_i, \vec{\omega}_r, \vec{\omega}_m)$  is defined as shown in Equation (2.12). By substituting  $f_{r(M)}(\vec{\omega}_i, \vec{\omega}_r, \vec{\omega}_m)$  from Equation(2.12) ,  $G(\vec{\omega}_i, \vec{\omega}_r, \vec{\omega}_m)$  from Equation(3.3) and  $D(\vec{\omega}_m)$  from Equation(3.4) into Equation(3.1), the reflectance model is obtained. However, the resulting integral can not be easily evaluated. Therefore, Oren and Nayar provided an approximation by using a identified basis function and conducting a large amounts of numerical simulations to evaluate this integral. The approximated expression of directly reflected part is following as:

$$\begin{aligned} f_r^{dir}(\theta_i, \theta_r, \varphi, \rho, \sigma) = & \frac{\rho}{\pi} [C_1(\sigma) + C_2(\theta_1, \theta_2, \varphi, \sigma) \cos(\varphi) \tan(\theta_2) \\ & + C_3(\theta_1, \theta_2, \sigma) (1 - |\cos(\varphi)|) \tan\left(\frac{\theta_1 + \theta_2}{2}\right)] \end{aligned}$$

where:

- $\rho$  is the albedo of each facet;
- $\varphi = |\varphi_i - \varphi_r|$  is the relative azimuth angle;
- $\theta_1 = \max(\theta_i, \theta_r)$  is the maximum zenith angle between  $\theta_i$  and  $\theta_r$ ;
- $\theta_2 = \min(\theta_i, \theta_r)$  is the minimum zenith angles between  $\theta_i$  and  $\theta_r$ ;
- $\sigma$  (in radians) is a parameter for the surface roughness, which is gaussian standard deviation in angles of the microfacets normal
- $C_1, C_2, C_3$  are constant:

$$C_1(\sigma) = 1 - 0.5 \frac{\sigma^2}{\sigma^2 + 0.33}$$

$$C_2(\theta_1, \theta_2, \varphi, \sigma) = \begin{cases} 0.45 \frac{\sigma^2}{\sigma^2 + 0.09} \sin(\theta_1), & \text{if } \cos(\varphi) \geq 0 \\ 0.45 \frac{\sigma^2}{\sigma^2 + 0.09} \left( \sin(\theta_1) - \left( \frac{2\theta_2}{\pi} \right)^3 \right), & \text{otherwise} \end{cases}$$

$$C_3(\theta_1, \theta_2, \sigma) = 0.125 \left( \frac{\sigma^2}{\sigma^2 + 0.09} \right) \left( \frac{4\theta_1 \theta_2}{\pi^2} \right)^2$$

In a V-cavity microfacet, apart from the shadowing and masking effects described in microfacet theory, light rays may also bounce between adjacent facets, as seen in Fig. 3.1(c). This phenomenon is referred to as inter-reflections. In the case of Lambertian surfaces, the energy in an incident light diminishes rapidly with each inter-reflection bounce [17]. Accordingly, Oren and Nayar consider only two bounces inter-reflections and neglect the subsequent bounces. Similar to direct illumination component, the multiple inter-reflections part is approximated as:

$$f_r^{ms}(\theta_i, \theta_r, \varphi, \rho, \sigma) = 0.17 \frac{\rho^2}{\pi} \frac{\sigma^2}{\sigma^2 + 0.13} \left( 1 - \frac{4\theta_2^2}{\pi^2} \cos(\varphi) \right)$$

Combining the directly reflected part and the multiple inter-reflections part, the complete expression of the ON BRDF is:

$$f_{r(ON)}(\theta_i, \theta_r, \varphi, \rho, \sigma) = f_r^{dir}(\theta_i, \theta_r, \varphi, \rho, \sigma) + f_r^{ms}(\theta_i, \theta_r, \varphi, \rho, \sigma)(\sigma) \quad (3.5)$$

Notice that this model reduces to Lambertian BRDF when the roughness  $\sigma = 0$ .

This model has been applied to road materials, such as plaster and white sand in [17], where it provides a good fit with experimental measurements, with the fitting parameters  $\rho = 0.9, \sigma = 30^\circ$  for the former and  $\rho = 0.8, \sigma = 35^\circ$  for the latter.

### 3.1.2 Cook Torrance BRDF

The specular reflection model of rough surfaces introduced by Cook and Torrance in 1982 has gained widespread attention [6, 17–20]. This model is also based on microfacet theory, where each facet is assumed to exhibit specular reflection, corresponding to Equation (2.13). Consequently, the BRDF of each microfacet  $f_{r(M)}(\vec{\omega}_i, \vec{\omega}_r, \vec{\omega}_m)$  presented in Equation(3.1) can be derived as:

$$\begin{aligned} f_{r(M)}(\vec{\omega}_i, \vec{\omega}_r, \vec{\omega}_m) &= \left| \frac{\partial \vec{\omega}_h}{\partial \vec{\omega}_i} \right| \frac{F_r(\vec{\omega}_i, \vec{\omega}_h) \delta(\vec{\omega}_m - \vec{\omega}_h)}{|\vec{\omega}_i \cdot \vec{\omega}_h|} \\ &= \frac{F_r(\vec{\omega}_i, \vec{\omega}_h) \delta(\vec{\omega}_m - \vec{\omega}_h)}{4 |\vec{\omega}_i \cdot \vec{\omega}_h|^2}, \end{aligned}$$

where  $\vec{\omega}_h$  is unit halfway vector, and defined as:  $\vec{\omega}_h = \frac{\vec{\omega}_i + \vec{\omega}_r}{|\vec{\omega}_i + \vec{\omega}_r|}$ . The term  $\left| \frac{\partial \vec{\omega}_h}{\partial \vec{\omega}_i} \right| = \frac{1}{4|\vec{\omega}_i \cdot \vec{\omega}_h|}$  is the jacobian of the reflection transformation [16, 21]. Putting this  $f_{r(M)}(\vec{\omega}_i, \vec{\omega}_r, \vec{\omega}_m)$  into Equation(3.1),

we can replace the integral by the integrand evaluated at  $\vec{\omega}_m = \vec{\omega}_h$  according to the delta dirac function  $\delta(\vec{\omega}_m - \vec{\omega}_h)$ . Thanks to  $\vec{\omega}_r \cdot \vec{\omega}_h = \vec{\omega}_i \cdot \vec{\omega}_h$ , we arrive the final expression of CT BRDF:

$$f_{r(CT)}(\theta_i, \varphi_i, \theta_r, \varphi_r) = \frac{F_r(\vec{\omega}_i, \vec{\omega}_h)G(\vec{\omega}_i, \vec{\omega}_r, \vec{\omega}_h)D(\vec{\omega}_h)}{4 \cos \theta_i \cos \theta_r} \quad (3.6)$$

Notice that inter-reflections are not taken into account in this model.

It is known that the geometric attention function  $G$  given in Equation (3.1) is dependent of microfacet profile. Two widely used microfacet profiles in this model are introduced: V-cavity and smith.

### V-cavity microfacet profile

In its original formulation, Cook and Torrance adapted the former profile [22]. Similar to the microfacet profile used in ON model, it represents the surface as a collection of symmetric V-cavity microfacet, leading to the same  $G$  function as Equation (3.3).

### Smith microfacet profile

The latter represents more realistic surface but is more complicated, as it assumes that the microfacets are not auto-correlated. More precisely, it represents a random set of microfacets instead of a continuous surface, where the heights and normals of the microfacets are independent random variables [16]. This implies that the term  $G$  due to masking and shadowing is independent of the normal orientation  $\vec{\omega}_m$  for non-backfacing normals. Therefore, the  $G$  function is separated into two independent functions: the local masking function and the distant masking function. The former function is the binary discard of backfacing microfacets  $\chi^+$ , and the latter one is the probability of occlusion by a distant point of the microfacet, which is independent of the local orientation  $\vec{\omega}_m$ .

A commonly used form of smith joint masking-shadowing function is given as:

$$G(\vec{\omega}_i, \vec{\omega}_r, \vec{\omega}_m) = \frac{\chi^+(\vec{\omega}_r \cdot \vec{\omega}_m)\chi^+(\vec{\omega}_i \cdot \vec{\omega}_m)}{1 + \Lambda(\vec{\omega}_r) + \Lambda(\vec{\omega}_i)}, \quad (3.7)$$

where  $\Lambda(\vec{\omega}_i)$  and  $\vec{\omega}_i$  are auxiliary functions, which arise naturally when the derivation of masking and shadowing is conducted in the slope domain. This term depends on the chosen distribution function  $D(\vec{\omega}_m)$ .

The **Beckmann distribution** and **GGX (also known as Trowbridge-Reitz)** distribution are two common microfacet distributions used in BRDF models to describe the statistical orientation

of microfacets. The former one is applicable for a wide of surface conditions from smooth to very rough. It is derived from a Gaussian slope distribution of microfacets:

$$D(\omega_m) = \frac{\chi^+(\vec{\omega}_m \cdot \vec{n})}{\pi \alpha^2 \cos^4(\theta_m)} \exp\left(-\frac{\tan^2(\theta_m)}{\alpha^2}\right) \quad (3.8)$$

It produces a more sharply peaked distribution near the surface normal and falls off more rapidly for grazing angles. Its associated  $\Lambda(\vec{\omega}_r)$  and  $\Lambda(\vec{\omega}_i)$  are:

$$\begin{aligned} \Lambda(\vec{\omega}_r) &= \frac{\text{erf}(a)-1}{2} + \frac{1}{2a\sqrt{\pi}} \exp(-a^2) \\ \Lambda(\vec{\omega}_i) &= \frac{\text{erf}(a')-1}{2} + \frac{1}{2a'\sqrt{\pi}} \exp(-a'^2) \end{aligned} \quad (3.9)$$

Where  $a = \frac{1}{\alpha \tan \theta_r}$  and  $a' = \frac{1}{\alpha \tan \theta_i}$ . A given approximated  $\Lambda(\vec{\omega}_r)$  explained in [16, 21] follows as:

$$\Lambda(\vec{\omega}_r) \approx \begin{cases} \frac{1-1.259a+0.396a^2}{3.535a+2.181a^2}, & \text{if } a < 1.6 \\ 0, & \text{otherwise} \end{cases}$$

The approximation of  $\Lambda(\vec{\omega}_i)$  can be obtained by replacing  $a$  with  $a'$ .

The latter is designed to have a heavier tail, implying that it decays more slowly at grazing angles. Its mathematical expression is given as:

$$D(\vec{\omega}_m) = \frac{\chi^+(\vec{\omega}_m \cdot \vec{n})}{\pi \alpha^2 \cos^4(\theta_m) \left(1 + \frac{\tan^2(\theta_m)}{\alpha^2}\right)^2} \quad (3.10)$$

Its corresponding  $\Lambda(\vec{\omega}_r)$  and  $\Lambda(\vec{\omega}_i)$  follows as:

$$\begin{aligned} \Lambda(\vec{\omega}_r) &= \frac{-1+\sqrt{1+\frac{1}{a^2}}}{2} \\ \Lambda(\vec{\omega}_i) &= \frac{-1+\sqrt{1+\frac{1}{a'^2}}}{2} \end{aligned} \quad (3.11)$$

Real-world road surface requires an accurate description of surface reflections which cannot be regarded in the traditional ON model. To address this limitation, this model is extended by a specular part, described by CT reflectance model using same v-cavity microfacet profile and the spherical gaussian distribution [6, 17, 18]. Linearly combining CT BRDF  $f_{r(CT)}(\theta_i, \varphi_i, \theta_r, \varphi_r)$  and ON BRDF  $f_{r(ON)}(\theta_i, \varphi_i, \theta_r, \varphi_r)$  using weighting factors, the new blended BRDF can be expressed as:

$$f_{r(ON-CT)}(\theta_i, \varphi_i, \theta_r, \varphi_r) = k_d f_{r(ON)}(\theta_i, \varphi_i, \theta_r, \varphi_r) + k_s f_{r(CT)}(\theta_i, \varphi_i, \theta_r, \varphi_r) \quad (3.12)$$

Where the weighting factors  $k_d$  and  $k_s$  are respectively for diffuse component and the specular component. This mixed model is employed for fitting the measured BRDF of the mixed-material road surfaces, such as asphalt [6], achieving a good agreement with measurements.

Another blended BRDF by mixing CT model and Lambertian model (Equation (2.12)) is employed for modelling the road material, such as blue or red concrete [18], exhibiting a good fit with the measured BRDF:

$$f_{r(\text{diffuse-CT})}(\theta_i, \varphi_i, \theta_r, \varphi_r) = k_d f_{r(\text{diffuse})}(\theta_i, \varphi_i, \theta_r, \varphi_r) + k_s f_{r(\text{CT})}(\theta_i, \varphi_i, \theta_r, \varphi_r) \quad (3.13)$$

## 3.2 Lafourture BRDF

A multifunctional empirical reflectance model introduced by Eric Lafourture and his collaborators in 1997 [23, 24], was used to fit measurements from realistic surface. This model is developed based on Phong model [24], decomposed in a sum of lobes, where each lobe represents a specific component of reflection (e.g., specular, diffuse, or retro-reflection):

$$f_{r(1\text{-lobe})}(\theta_i, \varphi_i, \theta_r, \varphi_r) = \rho \max \left( C_x \overrightarrow{\omega_r}_x \overrightarrow{\omega_i}_x + C_y \overrightarrow{\omega_r}_y \overrightarrow{\omega_i}_y + C_z \overrightarrow{\omega_r}_z \overrightarrow{\omega_i}_z \right)^n, \quad (3.14)$$

where  $\rho$  and  $n$  are the albedo and the specular reflectivity. The terms  $C_x, C_y, C_z$  are diagonal coefficients which can be seen as weighting the terms of the dot product  $\overrightarrow{\omega_r} \cdot \overrightarrow{\omega_i}$ . It is worth noting that  $C_x = C_y$  leading to isotropic directional-diffuse lobe, otherwise anisotropic. The term  $n$  represents the specular reflectivity. When  $n = 0$  and  $n \rightarrow \infty$ , this model corresponds to lambertian model and specular model, respectively. To represent a complex realistic reflectance functions, Lafourture computes a sum of several primitive functions presented in the form of Equation (3.14) by absorbing the albedo  $\rho$  and the other parameters:

$$f_{r(\text{Lafourture})}(\theta_i, \varphi_i, \theta_r, \varphi_r) = \max \left( \sum_i \rho_i [C_{x,i} \overrightarrow{\omega_r}_x \overrightarrow{\omega_i}_x + C_{y,i} \overrightarrow{\omega_r}_y \overrightarrow{\omega_i}_y + C_{z,i} \overrightarrow{\omega_r}_z \overrightarrow{\omega_i}_z]^{n_i}, 0 \right) \quad (3.15)$$

Where each primitive function  $i$  is defined by the parameters  $C_{x,i}$  ( $= C_{y,i}$ ),  $C_{z,i}$  and  $n_i$ . This model allows us to fit the measured BRDF of road surface in different status (e.g. dry and wet [24]), where the materials of roads are not specified. Furthermore, its mathematical formulation renders the model computationally efficient and relatively simple, making it a promising choice for fitting the measured BRDF in this study.

### 3.3 Retro-phong BRDF

In [25], a new extended Phong model was introduced by Spierings et al. in 2023. The authors took into account the effect of retro-reflection for road markings. In essence, this model is a linear combination of Lambertian reflector and Phong reflector:

$$f_{r(Retro-Phong)}(\theta_i, \phi_i, \theta_r, \phi_r) = \frac{k_d}{\pi} + \frac{k_s(\theta_i)(n+2)}{2\pi} (\vec{\omega}_{i_s} \cdot \vec{\omega}_r)^n + \frac{k_r(\theta_i)(n+2)}{2\pi} (\vec{\omega}_i \cdot \vec{\omega}_r)^n \quad (3.16)$$

Where  $k_d$ ,  $k_s$  and  $k_r$  are the parameters for diffuse component, specular component and retro-reflection component. To satisfy the principle of energy conservation, these three factors are subject to the following constraint:

$$k_d + k_s + k_r < 1$$

This model has been employed for 3 road marking materials [25] containing glass beads (SWARCOLimboplast D480 withMegalux 0.6-1.5 KT14, SWARCOLimboplast D480 with P21 3:1, 3MStamark A650), achieving a good fit with the measured results.

### 3.4 Hapke's SHOE BRDF model

A well-known semi-empirical BRDF model widely used for beach sand desert was developed by Hapke in the 1980s [26–28]. This model is based on radiative transfer theory and formally incorporated the Shadow Hiding Opposition Effect (SHOE), and typically expressed as:

$$f_{r(Hapke-SHOE)}(\theta_i, \varphi_i, \theta_r, \varphi_r) = \frac{\rho_{ss}}{4\pi} \frac{1}{\cos \theta_i + \cos \theta_r} \{[1 + B(g)] p(g) + H(\theta_i)H(\theta_r) - 1\}, \quad (3.17)$$

where:

- $\theta_i, \varphi_i$  are the incident zenith and azimuth angles.
- $\theta_r, \varphi_r$  are the emitted reflectance zenith and azimuth angles.
- $\rho_{ss}$  is the single scattering albedo.

- $g$  is the phase angle, which is the zenith angle difference between the incident direction and emitted reflectance direction.
- $B(g)$  is the opposition effect term specifically incorporates the SHOE:

$$B(g) = \frac{B_0}{1 + \frac{1}{h \tan(g/2)}}$$

- $B_0$  is the height of the backscatter peak;
- $h$  is width of the backscatter peak;
- $p(g)$  is the scattering phase function, which quantifies the angular distribution of scattered light relative to the direction of the incoming light.

In general, the scattering behaviors are usually classified into 3 types:

- forward scattering
- backward scattering
- isotropic (light is scattered equally in all direction, indicating  $p(\theta) = 1$ )

In the Henyey-Greenstein (HG) phase function expressed in the following equation, these behaviors are described by a single parameter  $\zeta$  (also called asymmetry factor), corresponding to  $\zeta > 0$ ,  $\zeta < 0$  and  $\zeta = 0$  respectively.

$$p(g) = p_{HG}(g) = \frac{1 - \zeta^2}{(1 + \zeta \cos(g) + \zeta^2)^{3/2}}$$

- $H(\theta)$  is the angular dependent function:

$$H(\theta) = \frac{1 + 2 \cos \theta}{1 + 2 \cos \theta \sqrt{1 - \rho_{ss}}}$$

To fit the measured BRDF, this model is required to find the 4 unknown parameters which are the SHOE backscatter parameters  $B_0$  and  $h$ , and the asymmetry factor  $\zeta$  and the single scattering albedo  $\rho_{ss}$ . This complicated parameterization may lead to high computation complexity and so expensive time cost. To address this, some researchers made minor modification by substituting the

product  $[1 + B(g)] p(g)$  of Hapke's SHOE model with a series expansion of Legendre Polynomials  $\left\{1 + \sum_{n=1}^N a_n P_n\right\}$ . As such, the final expression of this model becomes:

$$f_{r(Hapke-SHOE)}(\theta_i, \varphi_i, \theta_r, \varphi_r) = \frac{\rho_{ss}}{4\pi} \frac{1}{\cos \theta_i + \cos \theta_r} \left\{ \sum_{n=1}^N a_n P_n + H(\theta_i)H(\theta_r) \right\} \quad (3.18)$$

Where  $P_n$  represents the Legendre Polynomials of order  $n$  starting from 1, and the coefficient  $a_n$  is the parameter fit to the Measurements data. This modified model is also called as Hapke SPF BRDF model, which does not require the parameters  $B_0$  and  $h$ . In [27], this model was shown to exhibit a good fit with the measured data for desert sand (collected from Mountain Pass, California, USA), with incident zenith angles varying from  $0^\circ$  to  $70^\circ$  across the wavelength range of  $400 - 2400 nm$ .

# Chapter 4

## Measurements of Road Surface Optical Properties

Road surfaces are inherently heterogeneous owing to variations in material composition, aging, weathering, and surface texture. These variations cause spatial and temporal changes in reflectance characteristics that influence both the visual performance of lighting installations and the thermal behavior contributing to urban heat island effects. To better understand these changes, numerous field and laboratory optical measurements of road surface materials have been conducted in recent decades, focusing mainly on BRDF [6,17,18,25] and solar albedo [7,14,29,30]. The former quantifies the angular distribution of reflected light, which is critical for optimizing visibility, and the latter represents the fraction of solar reflected radiation which governs pavement thermal performance. This chapter provides the overview of the measurements conducted in the past twenty years in terms of BRDF and solar albedo of different materials of roads.

### 4.1 BRDF Measurements of Road Surface

In road surface analysis, BRDF measurements offer a detailed understanding of surface reflectance properties, that impacts not only human safety but also the performance of automated systems, such as LiDAR and camera-based sensors in autonomous vehicles.

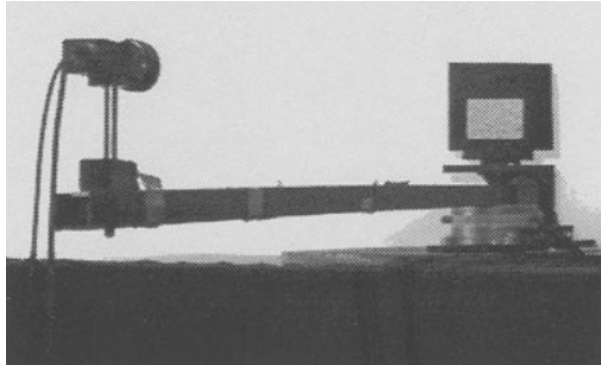
### 4.1.1 BRDF Measurement Set-up

The BRDF measurement systems for road surface can be broadly categorized into two types: laboratory-based and field-based approaches. The former is typically conducted under controlled environments where factors such as lighting, geometry, and surface conditions can be precisely controlled. The classic laboratory-based systems, such as gonioreflectometer [8, 17, 25] and goni-spectroradiometer if the detection is spectral [18, 27, 28], observe the same surface sample under varying observer and light source position, as seen in Fig. 4.1. They are commonly composed of the goniometer used to change the angles of incidence and detection (e.g. by rotating the robot swing arms [8, 17, 27], as seen in Fig. 4.1(a) and Fig. 4.1(c)), the light source and the detection sensors (e.g. camera, spectroradiometer). In many studies, halogen lamp is used as the light source due to its spectrum close to solar spectrums [8, 18, 25, 27, 28].

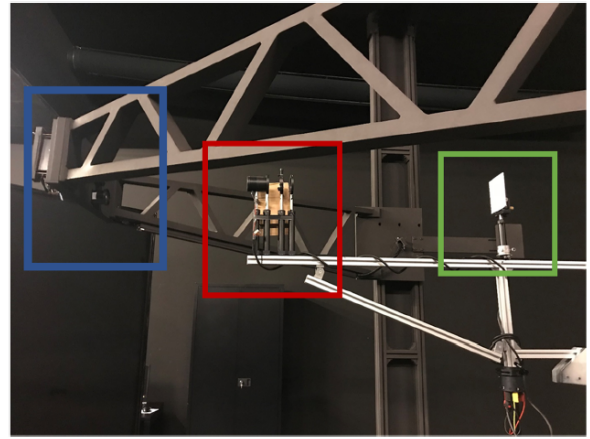
The latter is essential to obtain realistic data of road surface BRDF under actual environmental conditions, such as varying sunlight (from sunrise to sunset), weather (e.g. sunny, cloudy, rainy), and surface states (dry or wet). An example of such a setup is vehicle-based automotive measurement systems [6] (see in Fig. 4.2(a)), where natural sunlight serves as the light source and detection sensor, such as camera, is mounted on the car's front window. Apart from this set-up, the lab-based set-up presented in Fig. 4.1(c) is extended to measure the soil surface outside [27] by digging a small trench so that the pivot point of the pendulum arm coincided with the soil surface, as shown in Fig. 4.2(b)

### 4.1.2 Overview of BRDF Measurement of Different Road Materials

In practical applications, road surfaces like asphalt and concrete are commonly made from a combination of aggregates and binders. The optical properties of these road materials have been extensively studied to support accurate modeling. To evaluate the accuracy of their diffuse reflectance model developed in 1993 [17], Oren and Nayar conducted several experiments restricted to the visible spectrum, using road-like materials as test samples, such as plaster and white sand. Their experiment set-up is given in Fig. 4.1(a), where a  $512 \times 480$  pixel charged-coupled device (CCD) camera as receiver is mounted at the end of a 6 foot long beam and 300 Watt incandescent



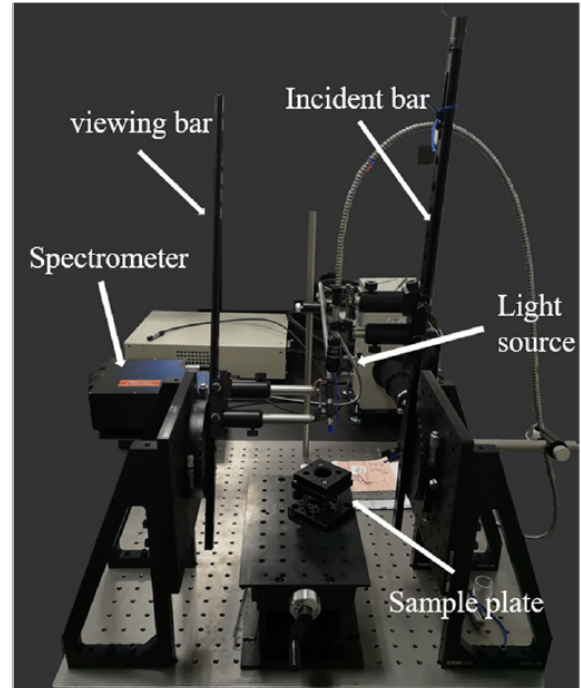
(a) Gonioreflectometer using a long beam



(b) Large near-field gonioreflectometer



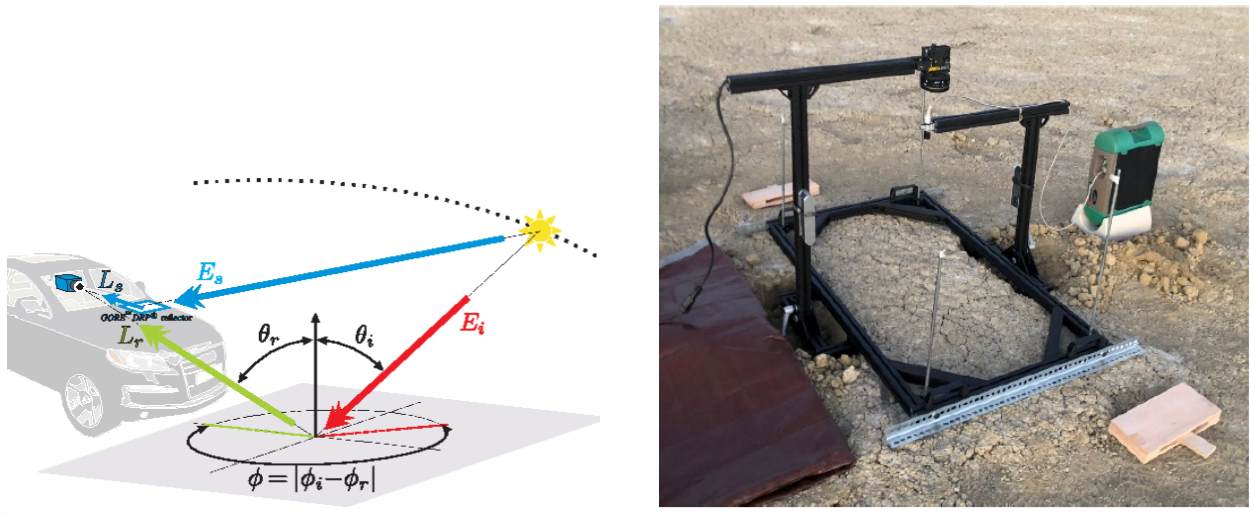
(c) Goni-spectroradiometer using 2 swing arms



(d) Goni-spectroradiometer using two bars

Figure 4.1: BRDF Laboratory measurement set-up

light source is used to illuminate the sample. A pair of fitting parameters of their BRDF model (ON Model as described in Section (3.1.1)), diffuse albedo  $\rho$  and surface roughness  $\sigma$  were empirically chosen to obtain the best fit with the measured radiance. The optimal parameter values were found to be  $\rho = 0.9$ ,  $\sigma = 30^\circ$  for plaster, and  $\rho = 0.8$ ,  $\sigma = 35^\circ$  for white sand, as shown in Fig. 4.3 and Fig. 4.4 respectively. In both figures, the solid lines and the dotted points respectively show the radiance predicted by ON model and the measured radiance. Notice that these measurements



(a) Vehicle-Mounted set-up

(b) Gonioreflectometer using 2 swing arms

Figure 4.2: BRDF Field-based measurement set-up

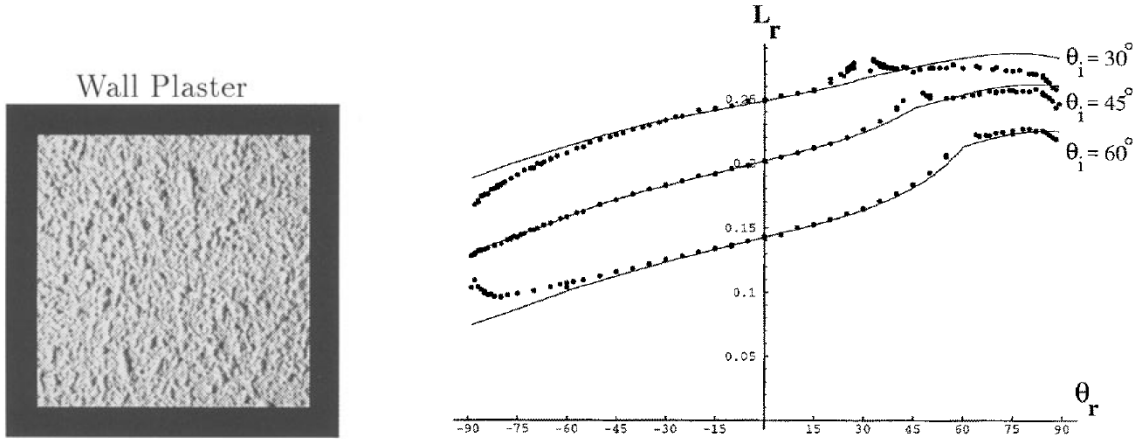


Figure 4.3: Plaster: Oren Nayar model fitting to measured radiance

were made in the plane of incidence ( $\varphi_r = \varphi_i$  and  $\varphi_r = \varphi_i + \pi$  corresponding to negative and positive values of  $\theta_r$ ). For both plaster and white sand, the measured radiance shows a clear peak in the specular direction, where the this model exhibits poor fitting performance. This indicates that ON model is not well-suited for capturing specular reflectance.

To compensate for this deficiency, Meister extended ON model by linearly combining it with a specular reflectance model (CT model as described in Section (3.1.2)) to fit spectral BRDF measurement for asphalt respectively at  $425\text{nm}$  and  $660\text{nm}$  over the period from 1995 to 2000 [18], as illuminated in Fig. 4.5. In addition, he also applied a mixed model which linearly combined Lam-

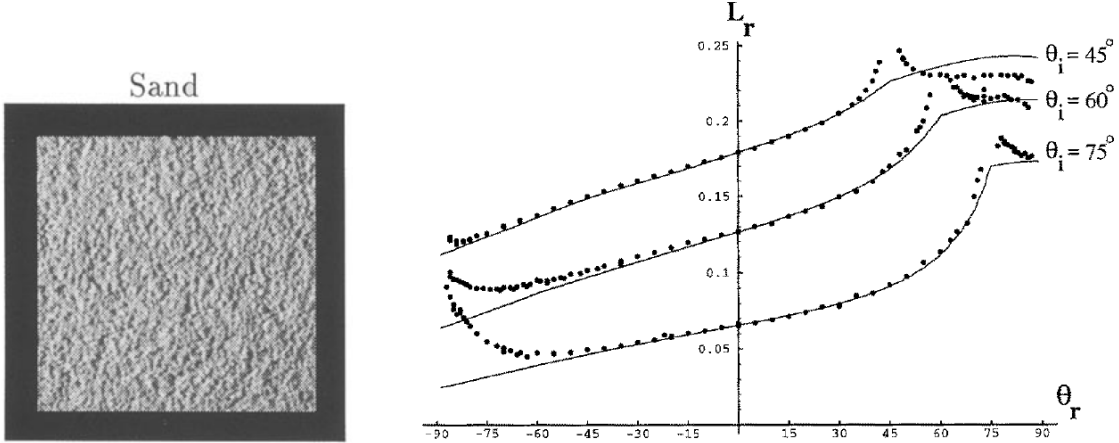


Figure 4.4: White sand: Oren Nayar model fitting to measured radiance

bertian model and CT model to fit the measured spectral BRDF of blue/red concrete respectively at the same wavelength, as shown in Fig. 4.6 and Fig. 4.7. These measurements were performed at the European Goniometric Facility (EGO) in Italy using a specially designed goniometer. Instead of employing a rotating robotic arm used by Oren and Nayar, this goniometer is constructed using two quarter arcs with a radius of 2 meters, which allow for the flexible mounting of a sensor and a light source [18]. To measure the spectral BRDF, this setup was modified by replacing the camera with an SE590 spectroradiometer, capable of capturing wavelengths in the range of 400 nm to 1100 nm. A 1000-watt halogen lamp was used as the light source due to its spectral similarity to sunlight. As observed from Fig. 4.5 to Fig. 4.7, the measured BRDFs were well fitted across most configurations.

In addition to the laboratory-based setup, Roser et al. conducted several experiments directly on natural concrete road surfaces using a three-dimensional geometric model of the automotive BRDF measurement system [6], as shown in Fig. 4.2. The camera with known orientation was mounted behind the windshield, and sunlight was serving as the sole source of illumination. This system leverages single grayscale images, integrated with GPS and vehicle heading data, to estimate the reflectance properties of small road patches under both dry and damp conditions. The resulting measured data were subsequently fitted using the extended ON reflectance model that is same as the one used by Meister, as seen in Fig. 4.8. This extended model and their parameters were able to successfully differentiate between different pavement reflection conditions.

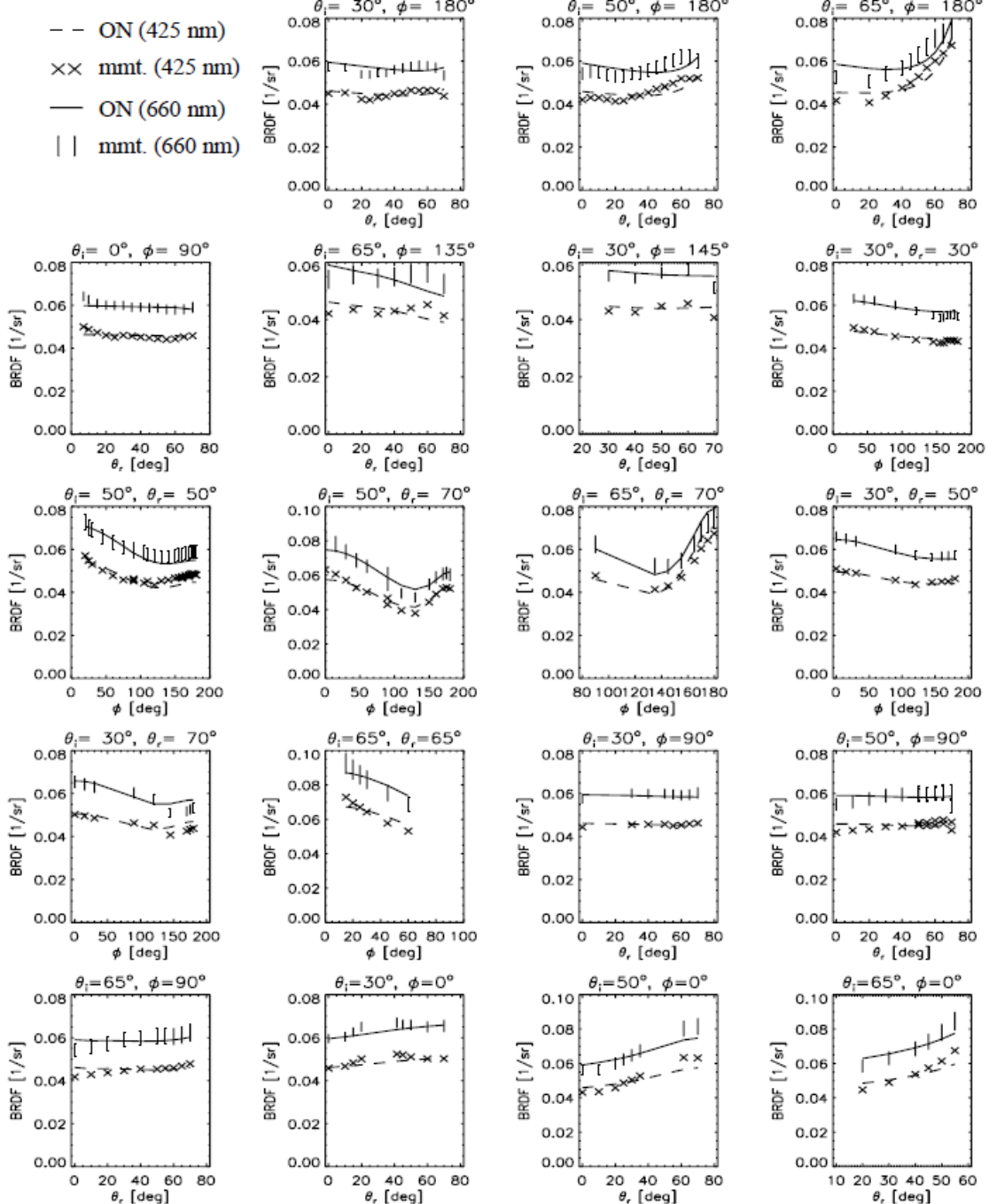


Figure 4.5: Asphalt: mixed reflectance model (ON + CT) fitting to measured BRDF

In recent years, Wise et al. conducted extensive measurements on beach sands under darkened conditions [27], using a goniometer-based setup shown in Fig.4.1(c) that was transitioned to field use as illuminated in Fig. 4.2(b). A spectroradiometer covering the  $400 - 2400\text{nm}$  range and a halogen lamp were employed in their experiments, and were mounted on a portable, manually

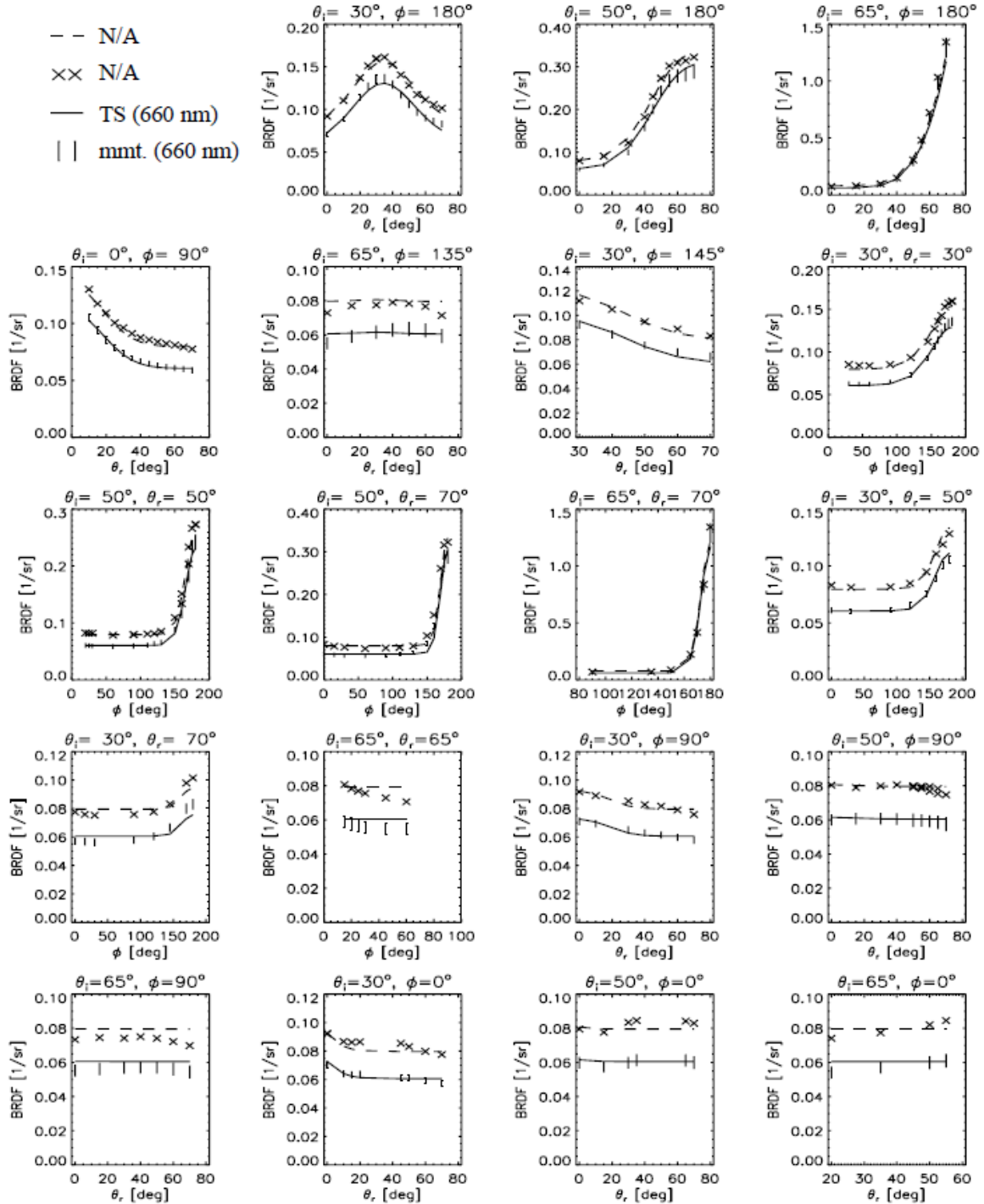


Figure 4.6: Blue concrete: mixed reflectance model (Lambertian + CT) fitting to measured BRDF

operated goniometer constructed from aluminum struts. In this goniometer design, the platform at the base measured  $122 \times 61\text{cm}$  and supported two swing arms, measuring  $46\text{cm}$  and  $66\text{cm}$  in length, with a total system weight of approximately  $9\text{kg}$ . It allows for measuring the spectral BRDF over

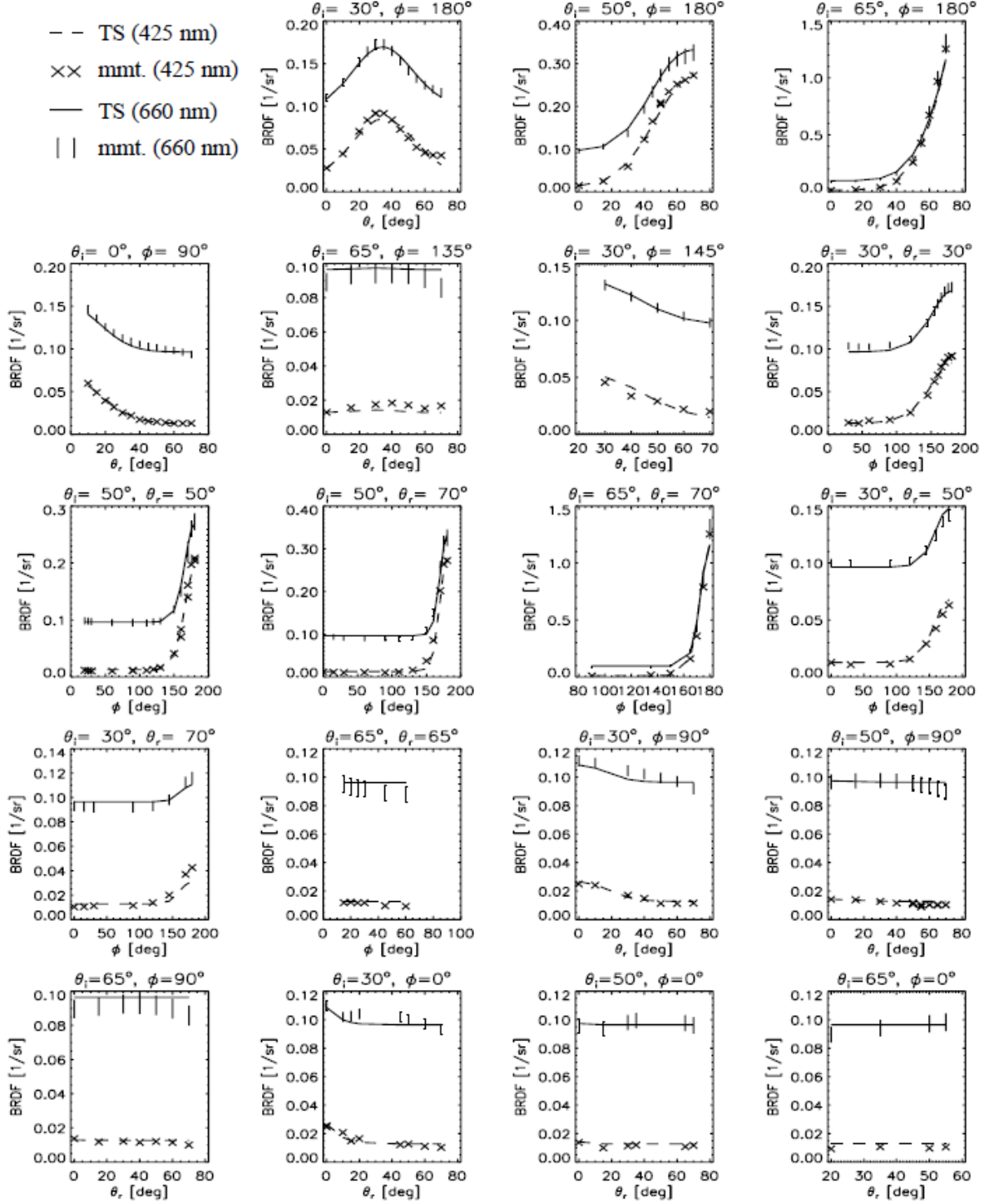


Figure 4.7: Red concrete: mixed reflectance model (Lambertian + TS) fitting to measured BRDF

a 140-degree range ( $-70^\circ$  -  $70^\circ$ ) to within 3 degrees of backscatter. These measured BRDF data were fitted using Hapke's SHOE model described in Section (3.4) wherein a series expansion of Legendre Polynomials was substituted for the angularly dependent backscatter function. The best-

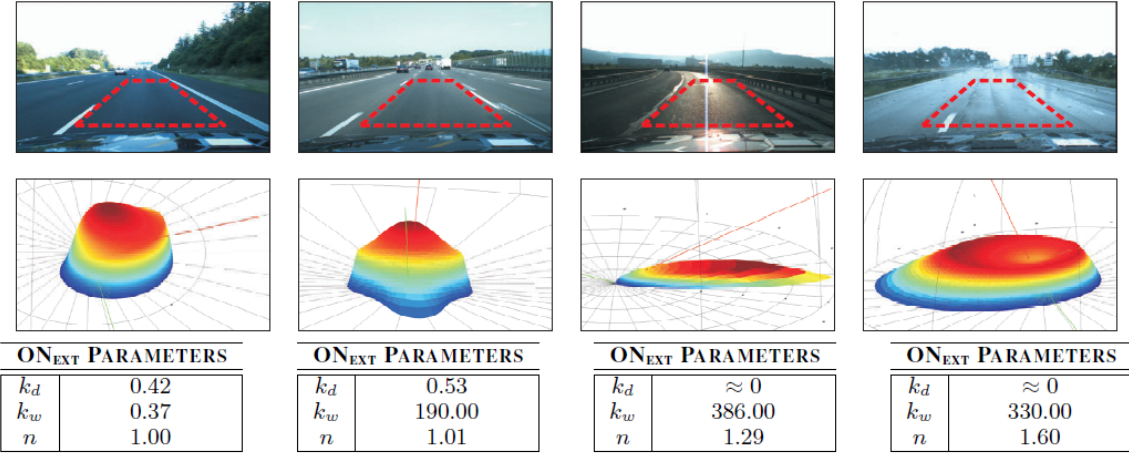


Figure 4.8: Concrete road: mixed reflectance model (ON + TS) fitting to measured BRDF

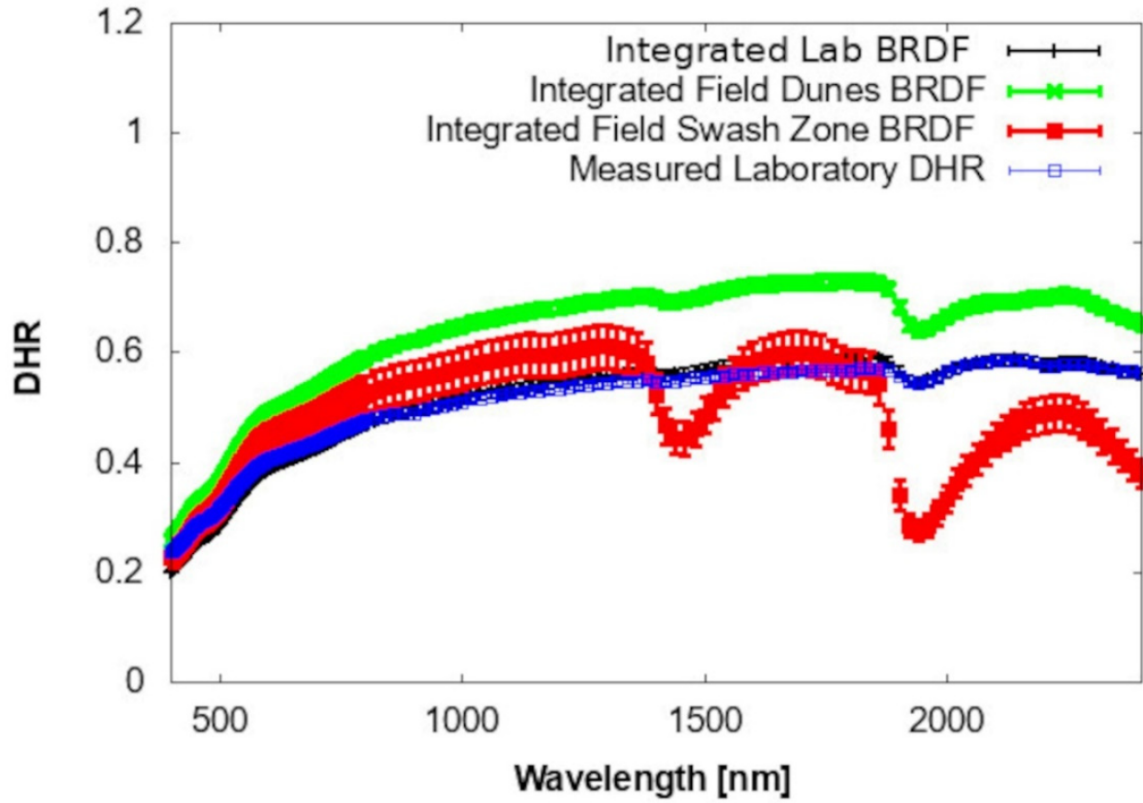


Figure 4.9: Chincoteague Island beach sand: Hapke's SHOE model fitting to measured DHR

fit model BRDF was then integrated over the hemisphere to compute the Directional Hemispheric Reflectance (DHR), as shown in Fig. 4.9. It can be observed that the integrated Lab BRDF (black) is almost overlapped with the measured DHR (blue), verifying the effectiveness of this BRDF model in capturing reflectivities of beach sands.

Apart from the beach sands, many spectral reflectance measurements on 13 different igneous rocks (seen in Fig.4.10) and their powders with different sizes in visible and near-infrared range from  $400\text{nm}$  to  $2500\text{nm}$  were performed by Zhuang et al. [28]. Similar to the experimental set-up in [27], the spectrometer and the light source were mounted on manually operated goniometer that consists of two rotary stages with bars, as shown in Fig. 4.1(d). This set-up design is capable of adjusting the viewing and the incident zenith angles from  $0^\circ$  to  $70^\circ$  continuously. To emit the spectrum from  $400\text{nm}$  to  $2500\text{nm}$ , the light source they utilized was highly stable Newport 66502-250Q-R1 quartz tungsten halogen lamp with an adjustable power range from 0-250W. The reflected light is collected by a bare fiber and transmitted to Spectral Evolution SR-2500 spectrometer. In their work, they measured respectively the intensities from the target sample and the reference Lab-sphere Spectralon plaque at incident zenith angle of  $0^\circ$  and a viewing zenith of  $30^\circ$ . Their ratio was considered as the relative reflectance, which is used to compute the reflectance factor (REFF) of this sample by multiplying the absolute Spectralon REFF values measured by RELAB [28]. These measurements were then fitted also using the Hapke's SHOE model, where the phase function is approximated by an empirical two-term Legendre polynomial. As illustrated in Fig. 4.11, the fitted spectral reflectance curves for some samples with particle sizes exceeding  $675\mu\text{m}$  are too similar to be clearly distinguished. It can also be observed that this model may not produce accurate spectral reflectance for all samples and particle sizes, likely due to its inherent simplicity and the assumption of a constant refractive index ( $n = 1.6$ ) irrespective of wavelengths.

Alongside studies on road materials, the optical properties of road markings have attracted increasing attention in recent years. Spieringhs et al. [25] carried out several experiments on three different types of road markings (seen in Fig. 4.12) using a Large Near-Field Goniometer (LNFG) developed by TechnoTeam, as shown in Fig.4.1(b). The elements highlighted in blue, red, and green boxes correspond to the luminance camera, the fixed light source, and the sample holder, respectively. In their measurements, a TechnoTeam LMK 98-4 high-tech calibrated luminance camera with a resolution of  $1390 \times 1040$  pixels was mounted in the RIGO801 LNFG, which can be moved freely in order to allow for measurements in all desired viewing angles. Then the camera and the RIGO801 LNFG are connected to the computer in order to set the position of the arm of the LNFG via the TechnoTeam software and to record the luminance images. A QTH10(/M)

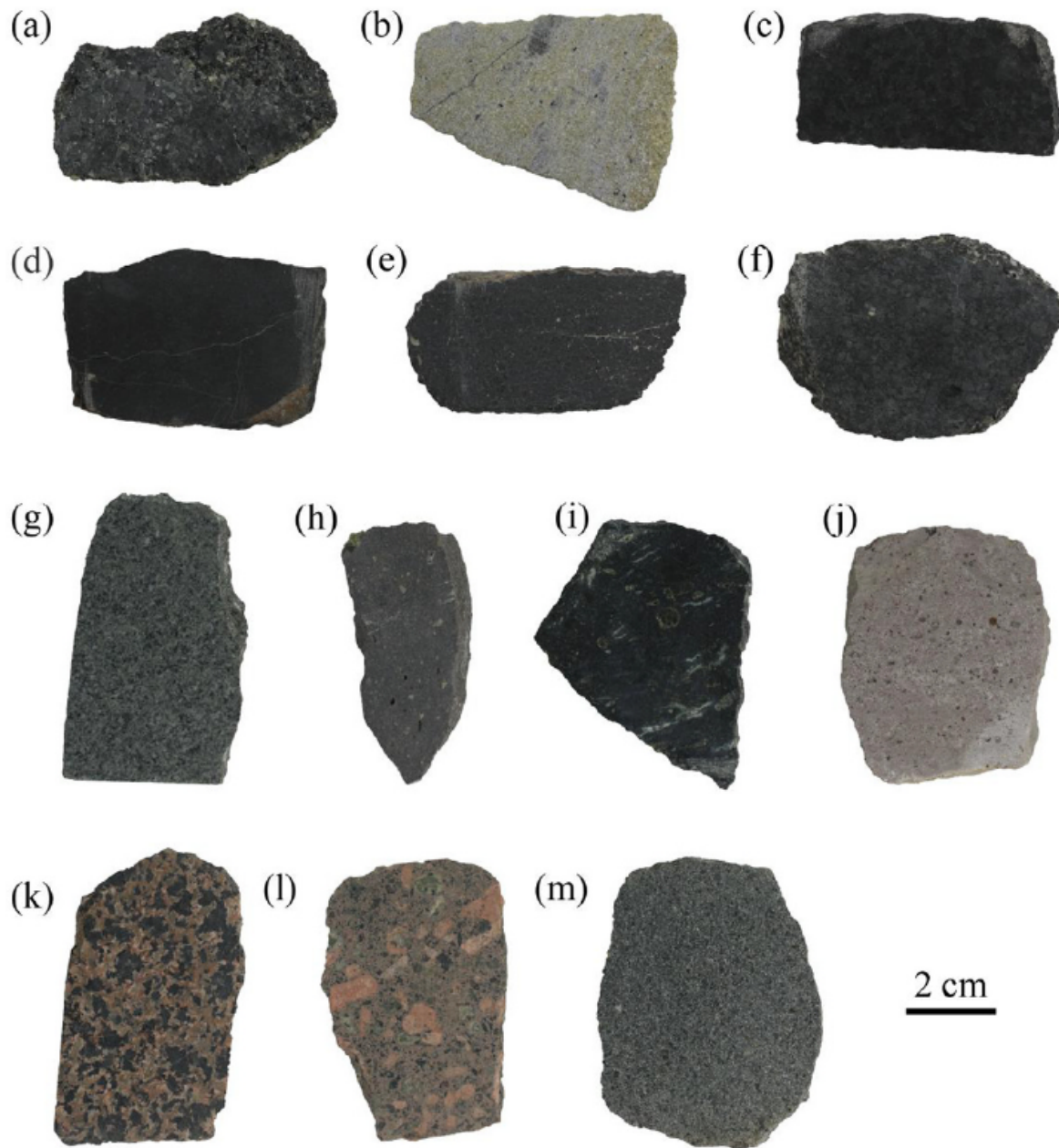


Figure 4.10: 13 igneous rocks slabs with a thickness of 1.5 cm: (a) Dunite; (b) Peridotite; (c) Olivine pyroxenolite; (d) Picrite porphyrite; (e) Kimberlite; (f) Gabbro; (g) Diabase; (h) Olivine basalt; (i) Andesite basalt; (j) Trachyte; (k) Pyroxenite syenite; (l) Orthophyre; (m) Lamprophyre.

Quartz Tungsten-Halogen 50W 12V lamp with a broadband emission between 400 and 2200nm was employed as light source and connected to programmable Delta Elektronika SM1500 DC power system. Notice that the position of light source is fixed, indicating that it is impossible to allow

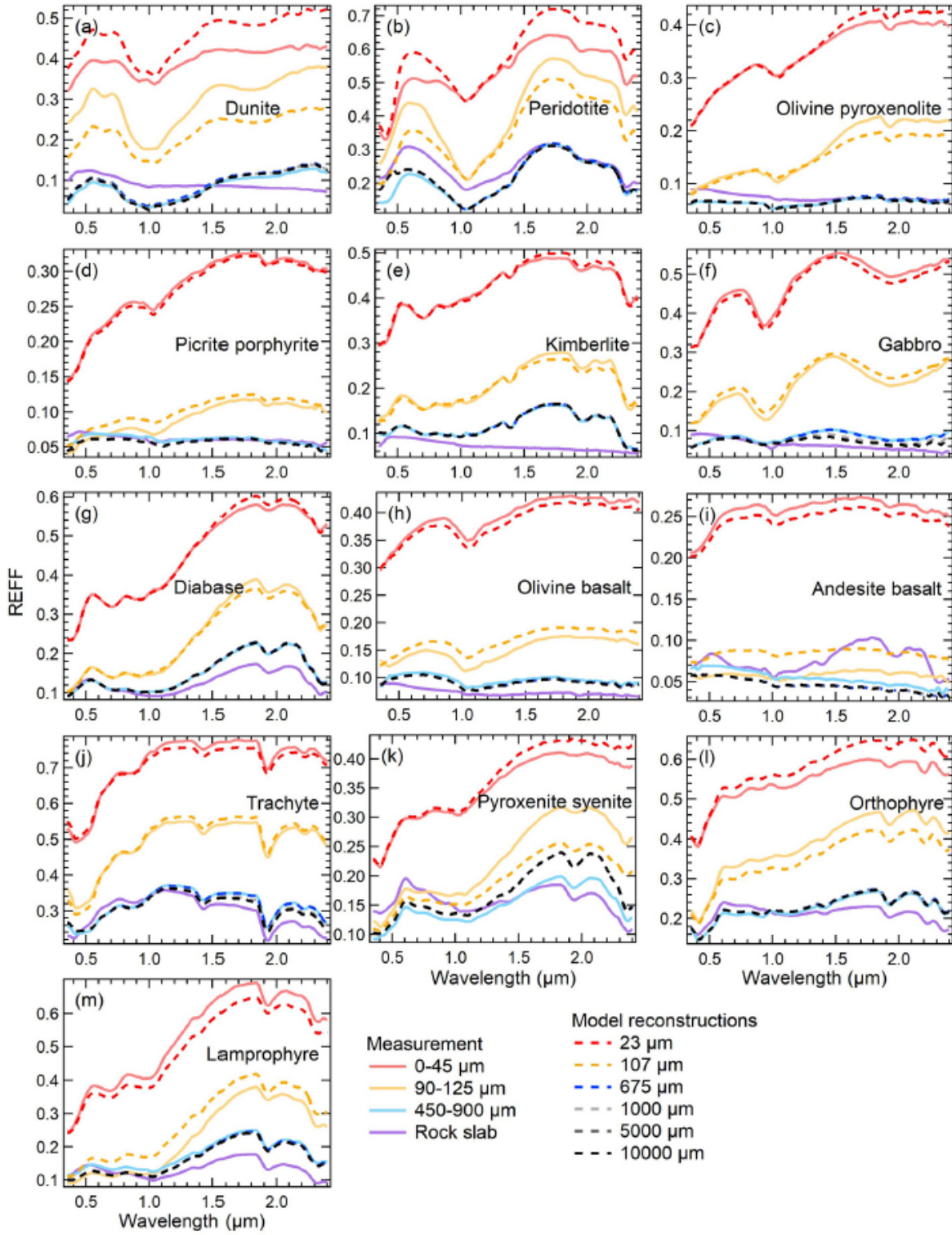


Figure 4.11: Igneous rocks: Hapke's SHOE model fitting to measured REFF

for all desired incident angles ( $\theta, \varphi$ ) by changing the position of light source. To accommodate this, an adjustable sample holder was designed to enable rotation around both vertical and hori-



Figure 4.12: Three road marking samples containing glass beads: (1) SWARCO Limboplast *D*480 with Megalux 0.6 – 1.5 KT14, (2) SWARCO Limboplast *D*480 with *P*21 3 : 1, and (3) 3MStamark *A*650.

zontal axes. These measured data for 3 road markings were shown in Fig. 4.13. As the incident angle  $\theta_i$  increases, retro-reflection and specular reflection become more pronounced. Particularly at  $\theta_i = 80^\circ$ , the BRDF in the retro-direction nearly reaches or exceeds 1. To able to predict the BRDF at any incident angles  $(\theta_i, \varphi_i)$  and viewing angles  $(\theta_r, \varphi_r)$ , the authors employed the retro-phong model (described in Section (3.3)) to fit the measurements. A fitting example for road marking sample 1 was presented in Fig .4.14. Compared to the other models evaluated in [25], this model demonstrated better fitting performance.

## 4.2 Solar Albedo Measurements of Road Surface

### 4.2.1 Albedo Measurement set-up

In literature, there exist two approaches to measure the solar albedo: laboratory-based and filed-based [14]. The former is carried out indoors using a spectrophotometer equipped with integrating spheres, as following the standard test ASTM E903. The goal is to obtain the spectral reflectance which is an approximate estimate of solar albedo. This kind of test method is applicable to

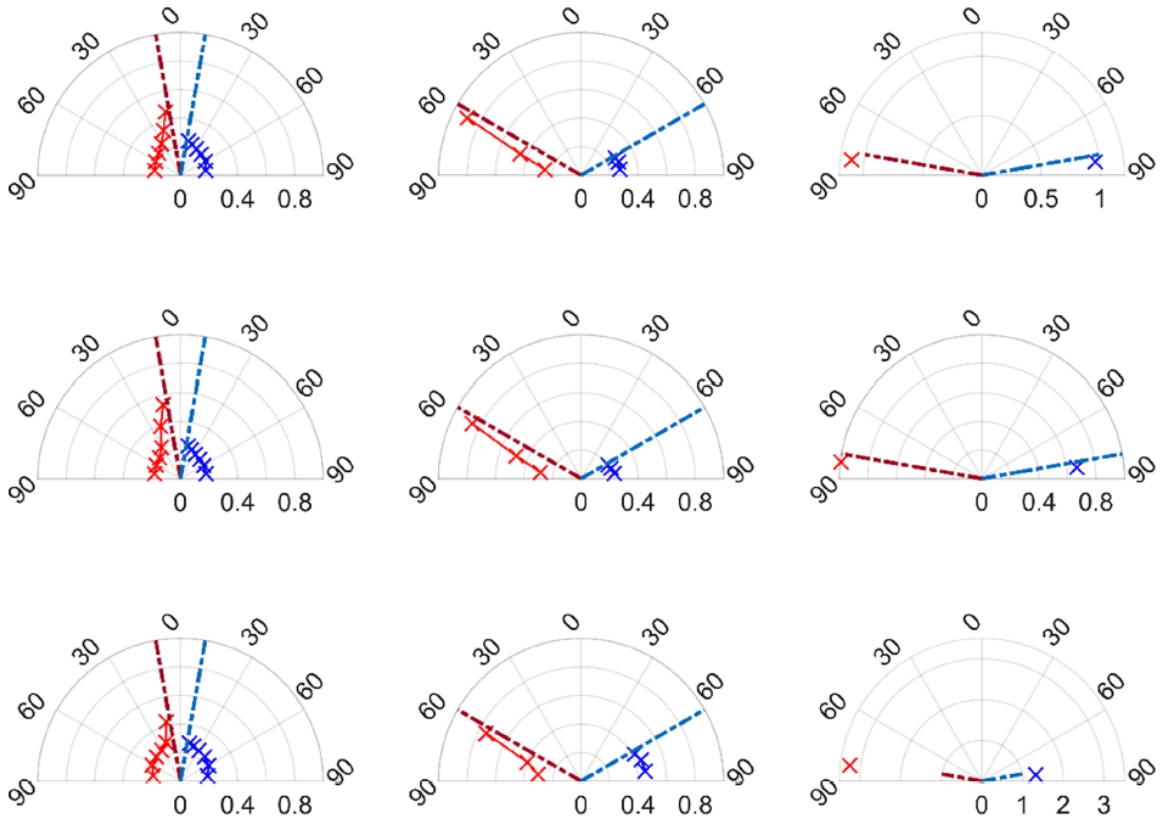


Figure 4.13: Measured BRDF: Top row for sample 1, middle row for sample 2, bottom row for sample 3. The 3 plots in a row represent an incident angle of  $\theta_i = 0^\circ, 60^\circ, 80^\circ$  for a fixed  $\varphi_i$  from left to right, respectively. The crosses and dashed lines in red represent the retro-reflective hemisphere, and the ones in blue represent the specular hemisphere. The red dotted lines indicate the incident vectors. The radius of the polar diagrams is in  $sr^\circ$ .

materials having both specular and diffuse optical properties.

While the latter is following ASTM 1918, providing a realistic measure of solar albedo, but highly depending on the weather conditions. It is conducted outside using an albedometer composing of sky-facing and target-facing pyranometers parallel to the test surface, as seen Fig. 4.15, which are used to measure the incoming and reflected solar radiation respectively. The two pyranometers are mounted on an arm and a stand that centers the sensor at a height of 500mm above the target surface in order to minimize the effects of sensor, arm, and stand shadows on measured reflected radiation. The horizontal distance from the center of the pyranometer to the edge of the test surface has to be at least 2m. Besides, the arm and stand should be strong and cast the

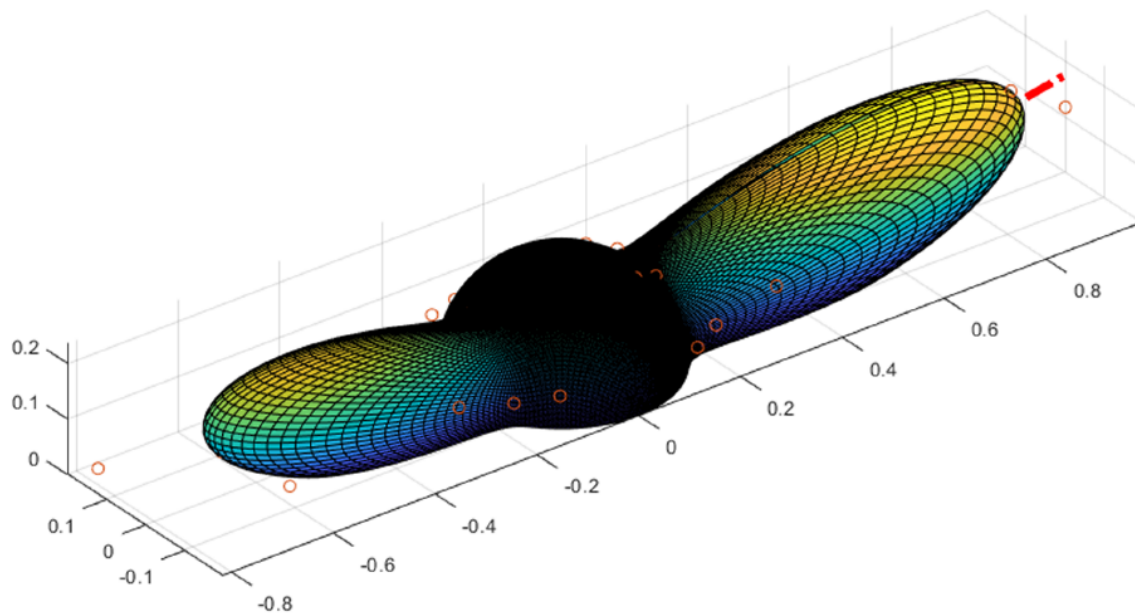


Figure 4.14: Road marking sample 1 (SWARCO Limboplast D480 withMegalux 0.6 – 1.5 KT14): Retro-Phong model fitting to measured BRDF. The dashed lines indicate the incident direction, the colored grids represent the fitted BRDF, the dots indicate the measured BRDFs in different viewing angles

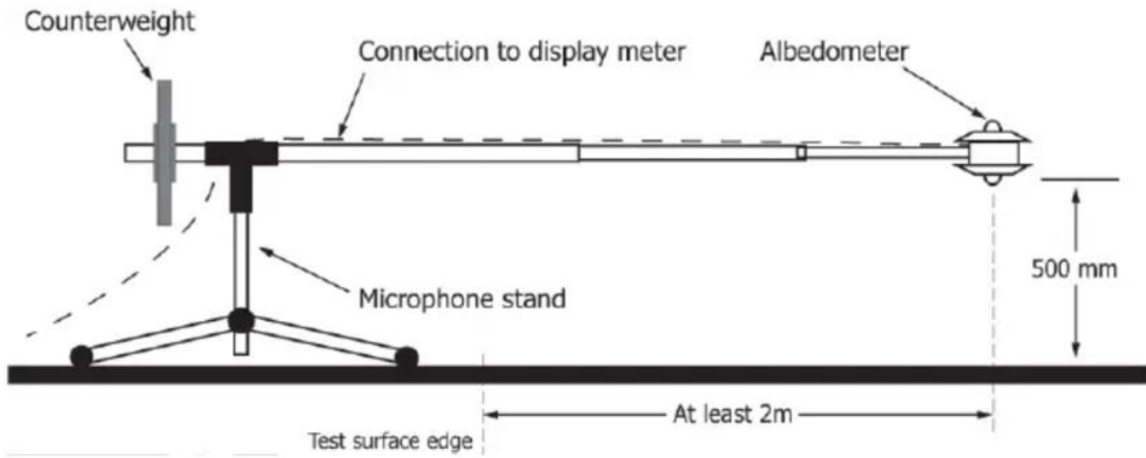


Figure 4.15: Schematic of the Albedometer and Its Support (provided in ASTM 1918-21)

smallest possible shadow. This test method applies to low-sloped surface which are at least 4m in diameter (if circular) or at least 4m on each side (if rectangular). Notice that the angle of the sun to the normal of the test surface should be less than 45°. Due to horizontal and low-sloped surfaces, the hours in summer for this test should be between 9.a.m and 3.p.m local standard

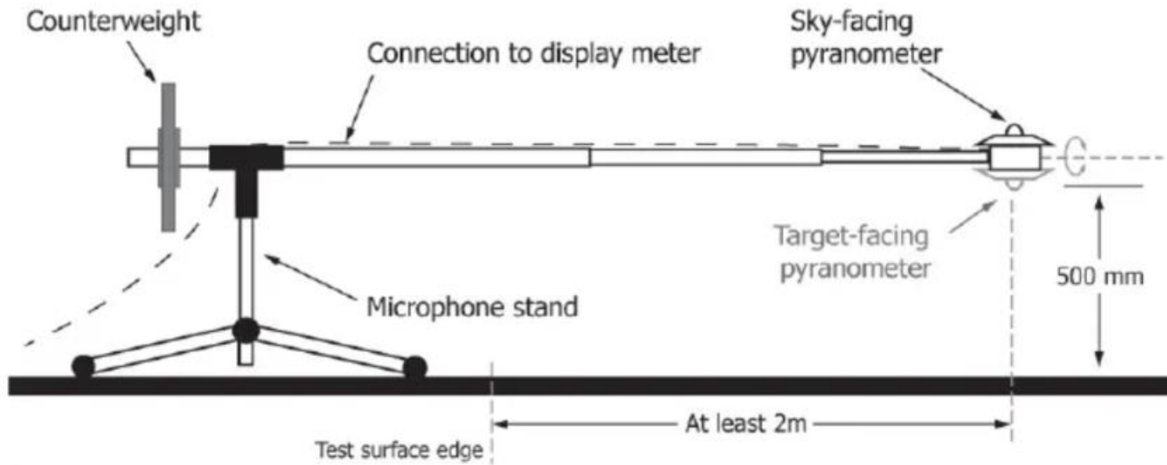


Figure 4.16: Schematic of the Pyranometer and Its Support (provided in ASTM 1918-21)

time, which is when solar radiation is at least 70% of the value obtained at noon for that day. In winter, conducting the test should be between 10.a.m and 2.p.m local time, considering low solar incident angle. The albedometer will read both the incoming solar radiation and the reflected solar radiation simultaneously. To ensure the accuracy, each reading should be constant for at least 10s before recording the its values. Plus, at least 3 pairs of incoming and reflected radiation are required to be measured within 2 minutes. The calculated solar reflectance which is the ratio of the reflected radiation to the incoming radiation need to agree to within 0.01 in a reflectivity scale of 0 to 1.

The field-based method can be conducted using only a pyranometer, as illustrated in Fig. 4.16. Initially, the pyranometer is positioned facing upward and parallel to the test surface to measure the incoming solar radiation. After this measurement, the device is flipped to face downward to capture the reflected radiation. This reading process is quite similar to that of an albedometer. However, there is a key distinction due to time delay between reading incoming and reflected radiation. Unlike the albedometer, it requires at least three pairs of measurements of incoming and reflected radiation taken within a span of 10 minutes to ensure accuracy and reliability in the results for this one-pyranometer set-up.

#### 4.2.2 Overview of Solar Albedo Measurements on Road Surfaces

# Chapter 5

## Simulation and Measurement of single-component road sample

### 5.1 Methodology

#### 5.1.1 Preparation of single-material road samples

Explain what materials are chosen for measurement

Aggregate 1

Aggregate 2

Aggregate 3

Aggregate 4

the process to fabricate the single-component road sample

#### 5.1.2 Measurement set-up: the Gonioreflectometer at Cerema

The Gonioreflectometer is composed of:

- light source: Halogene lamp (350nm -2500nm)
- reception sensor: spectroradiometer

- goniometer: changing the incident angle and viewing angles

#### Measurement scenario

- $l$  - the horizontal distance between the sample and the spectroradiometer
- $H$  - the height difference between spectroradiometer and the sample
- $\gamma$  - the incident angle ( $\gamma = \theta_i$ ):  $0^\circ - 90^\circ$
- $\alpha$  - the observation angle ( $\alpha = \frac{\pi}{2} - \theta_r$ ):  $0^\circ - 90^\circ$
- $\beta$  - the angle between the vertical planes of illumination and observation ( $\beta = \pi - (\phi_r - \phi_i)$ )
- $\delta$  - the angle between the observation plane and the roadway (x) axis ( $\delta = \phi_r - \pi$ )

#### Measurement steps

In this study, we aim to develop a comprehensive model by blending reflectance models of individual components that constitute a given road surface, to fit the measured BRDF data. Therefore, BRDF measurements will be conducted indoors using a gonioreflectometer developed by Cerema (see in Fig. 5.1), allowing for the elimination of environmental interferences and ensuring precise control over experimental conditions.

- step 1 - installation of the spectroradiometer

There are several spectroradiometers:  $1^\circ$  and  $5^\circ$

- step 2 - installation of the sample
- step 3 - launch the software (GonioPilotageDesAxes) to turn on the Halogene lamp

When the software is on, then in this software

1. set the parameters
  - choose COM3
  - choose where to save the result files
2. turn on COM ESP301 (green means it is on)



Figure 5.1: Gonioreflectometer (Cerema)

3. turn on the lamp (green means it is on)
  4. access the measured screen
  5. activate the remote control (yellow mean it is on)
- step 4 - launch python code to start the measurement
    1. modify the  $\alpha$ , and change the saving sql file name for corresponding  $\alpha$
    2. change the height of spectroradiometer
    3. launch the spectral evolution
    4. launch the python codes
    5. once the python codes is done, stop the spectral evolution
  - step 6 - send sql file and measured radiance to Sebastian and receive the results in .csv file

Measurement set-up:

Provide the diagram of measurement set-up.

### **5.1.3 Fitting methods**

introduce the fitting methods: gradient descent, levenberg-Marquardt etc

## **5.2 Results**

### **5.2.1 Result of Lazard 2/6**

### **5.2.2 Result of Lazard 6/10**

### **5.2.3 Result of Sand**

### **5.2.4 Result of**

# **Chapter 6**

## **Simulation and measurement of multi-component road sample**

### **6.1 Existing methods of mixing BRDF**

This section presents the methods to mix the BRDF, linear or non-linear combination of two or more BRDFs

### **6.2 Proposed methods**

Present the method to model the multi-component road samples

### **6.3 Results**

#### **6.3.1 Methodology**

Provide several samples which have different combination of multiple component with detailed size, portion, materials:

Road sample 1:

Road sample 2:

Road sample 3:

Road sample 4:

### **6.3.2 Result of road sample 1**

### **6.3.3 Result of road sample 2**

### **6.3.4 Result of road sample 3**

### **6.3.5 Result of road sample 4**

# **Chapter 7**

## **Conclusion and Perspectives**

### **7.1 Conclusion**

### **7.2 Perspectives**

# Bibliography

- [1] Valérie Muzet, Sébastien Liandrat, Vincent Bour, Jérôme Dehon, and Jean-Pierre Christory. Is it possible to achieve quality lighting without considering the photometry of the pavements? In *Conference CIE 2021, NC Malaysia*, pages 11–25, 2021.
- [2] Valérie Muzet, Florian Greffier, Aurélia Nicolaï, Alexandre Taron, and Paul Verny. Evaluation of the performance of an optimized road surface/lighting combination. *Lighting Research & Technology*, 51(4):576–591, 2019.
- [3] Giuseppe Rossi, Paola Iacomussi, and Michele Zinzi. Lighting implications of urban mitigation strategies through cool pavements: energy savings and visual comfort. *Climate*, 6(2):26, 2018.
- [4] Tomasz E Burghardt, Harald Mosböck, Anton Pashkevich, and Mario Fiolić. Horizontal road markings for human and machine vision. *Transportation research procedia*, 48:3622–3633, 2020.
- [5] Wojciech Jarosz. *Efficient Monte Carlo methods for light transport in scattering media*. University of California, San Diego, 2008.
- [6] Martin Roser and Philip Lenz. Camera-based bidirectional reflectance measurement for road surface reflectivity classification. In *2010 IEEE Intelligent Vehicles Symposium*, pages 340–347. IEEE, 2010.
- [7] Berlian KUSHARI and Kunawee KANITPONG. Surface albedo of bangkok roads. In *Proceedings of the Eastern Asia Society for Transportation Studies Vol. 8 (The 9th International Conference of Eastern Asia Society for Transportation Studies, 2011)*, pages 181–181. Eastern Asia Society for Transportation Studies, 2011.

- [8] Mathieu Hébert. *Optical models for material appearance*. EDP Sciences Les Ulis, France, 2022.
- [9] Fred E Nicodemus. Directional reflectance and emissivity of an opaque surface. *Applied optics*, 4(7):767–775, 1965.
- [10] Rosana Montes and Carlos Ureña. An overview of brdf models. *University of Grenada, Technical Report LSI-2012-001*, 2012.
- [11] Matt Pharr, Wenzel Jakob, and Greg Humphreys. Physically based rendering: From theory to implementation. 2016.
- [12] Jiří Filip. Analyzing and predicting anisotropic effects of brdfs. In *Proceedings of the ACM SIGGRAPH Symposium on Applied Perception*, pages 25–32, 2015.
- [13] Ying Qu, Shunlin Liang, Qiang Liu, Tao He, Suhong Liu, and Xiaowen Li. Mapping surface broadband albedo from satellite observations: A review of literatures on algorithms and products. *Remote Sensing*, 7(1):990–1020, 2015.
- [14] Jun Chen, Zheng Zhou, Jiantao Wu, Shuguang Hou, and Mengcheng Liu. Field and laboratory measurement of albedo and heat transfer for pavement materials. *Construction and Building Materials*, 202:46–57, 2019.
- [15] Paola Iacomussi, Giuseppe Rossi, et al. Influence of material characterization in the design of tunnel lighting installations. In *CIE Washington 2019*, pages 546–552. 2019.
- [16] Eric Heitz. Understanding the masking-shadowing function in microfacet-based brdfs. *Journal of Computer Graphics Techniques*, 3(2):32–91, 2014.
- [17] Michael Oren and Shree K Nayar. Generalization of the lambertian model and implications for machine vision. *International Journal of Computer Vision*, 14:227–251, 1995.
- [18] Gerhard Meister. *Bidirectional reflectance of urban surfaces*. PhD thesis, Staats-und Universitätsbibliothek Hamburg Carl von Ossietzky, 2000.

- [19] Simon Lucas, Mickaël Ribardi  re, Romain Pacanowski, and Pascal Barla. A micrograin bsdf model for the rendering of porous layers. In *SIGGRAPH Asia 2023 Conference Papers*, pages 1–10, 2023.
- [20] Simon Lucas, Micka  l Ribardi  re, Romain Pacanowski, and Pascal Barla. A fully-correlated anisotropic micrograin bsdf model. *ACM Transactions on Graphics*, 43(4):111, 2024.
- [21] Bruce Walter, Stephen R Marschner, Hongsong Li, and Kenneth E Torrance. Microfacet models for refraction through rough surfaces. *Rendering techniques*, 2007:18th, 2007.
- [22] Robert L Cook and Kenneth E. Torrance. A reflectance model for computer graphics. *ACM Transactions on Graphics (ToG)*, 1(1):7–24, 1982.
- [23] Eric PF Lafourche, Sing-Choong Foo, Kenneth E Torrance, and Donald P Greenberg. Non-linear approximation of reflectance functions. In *Proceedings of the 24th annual conference on Computer graphics and interactive techniques*, pages 117–126, 1997.
- [24] Nicolas Gimonet, Aur  lien Cord, and Guillaume Saint Pierre. How to predict real road state from vehicle embedded camera? In *2015 IEEE Intelligent Vehicles Symposium (IV)*, pages 593–598. IEEE, 2015.
- [25] Rik Marco Spieringhs, Jan Audenaert, Kevin Smet, Ingrid Heynderickx, and Peter Hanselaer. Road marking brdf model applicable for a wide range of incident illumination conditions. *JOSA A*, 40(3):590–601, 2023.
- [26] Bruce Hapke. Bidirectional reflectance spectroscopy. *Icarus*, 59(1):41–59, 1984.
- [27] John E Wise and John C Mars. Field reflectance measurements at night of beach and desert sands within a particulate brdf model. *Remote Sensing*, 14(19):5020, 2022.
- [28] Yan Zhuang, Hao Zhang, Pei Ma, Te Jiang, Yazhou Yang, Ralph E Milliken, and Weibiao Hsu. Visible and near-infrared reflectance spectra of igneous rocks and their powders. *Icarus*, 391:115346, 2023.
- [29] M Blumthaler and W Ambach. Solar uvb-albedo of various surfaces. *Photochemistry and photobiology*, 48(1):85–88, 1988.

- [30] Ruiqiang Bai, Mingyi Zhang, Jiwei Wang, Guanji Li, and Zhilang You. Study on the solar albedo characteristics of pavement and embankment slope surfaces in permafrost regions. *Solar Energy*, 237:352–364, 2022.